Hydrodynamic Loading of Dutch terraced houses due to flood actions using Computational Fluid Dynamics:

Validation and Demonstration

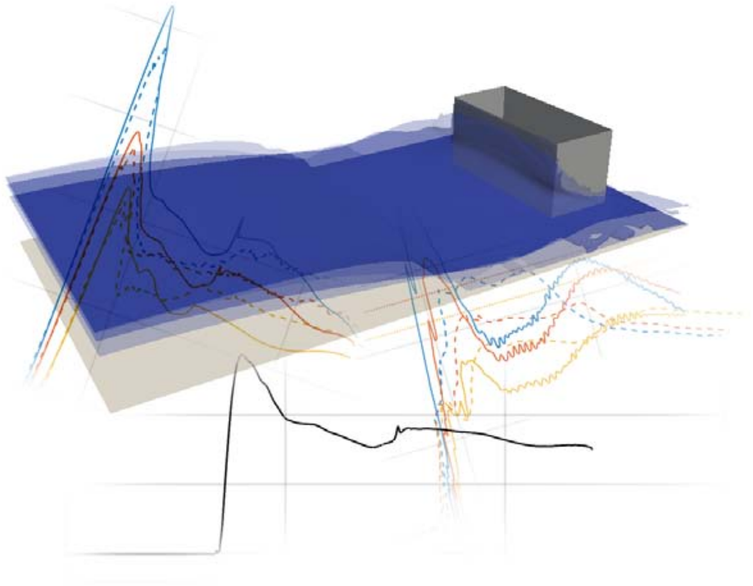

Hydrodynamic Loading of Dutch terraced houses due to flood actions using Computational Fluid Dynamics: Validation and Demonstration

Additional project thesis

within the Master's programme "Civil Engineering"

3rd September 2019 – 5th December 2019

Benedikt Bratz (B. Sc.)

Student Number: 5157749

TU Delft

Dr. Ir. Jeremy Bricker

Dr. Ir. M. A. Diaz Loaiza

Ir. P. A. Korswagen Eguren

ABSTRACT

Whenever a region - especially the coastal area - is affected by flood risk, it is essential for residential and life protection to gain knowledge about the mechanisms leading to the collapse of houses. There are empirical mortality functions to predict the mortality of population in the Netherlands directly affected by flooding, but due to probable changes in building quality it is necessary to investigate the fragility of the current building stock. For a detailed structural research containing collapse mechanisms, the resulting loads on buildings in case of flooding – depending on flow velocity, water height, building orientation, width, height etc. – should be known.

In current research, several physical experiments have been conducted in order to gain information about hydrodynamic loads on houses in flood actions. The present project aims to set up a numerical model for assessing the flow-induced pressure loads on residences. The model is based on physical experiments already conducted in model scale: a dam break wave is generated, impacting on a model residence of typical Dutch dimensions; then the flow-induced pressure loads are determined. The focus is on the quasi-steady flow part after the initial wave impact. For moderate computational load Reynolds-averaged equations are used for the numerical model. The generated flow conditions and load magnitudes are compared to physical results in order to validate the numerical model. It can be shown that the results generated during the quasi-steady flow part conform with physical results largely. Appearing discrepancies may result from model constraints regarding strongly mixed interface regions of air and water. Finally, possible further model applications are demonstrated: the effect of urban density (realised by blockage ratio variation) on the resulting load is investigated; in addition, the experiment is scaled to prototype scale. Generally, the numerical model serves as a useful tool for load estimation induced by the quasi-steady part of a dam break wave. The model can be used to investigate further modifications; a large range of input variables like e.g. flow conditions, residence geometries, residence arrangements can be assessed to gain information about main interrelations or specific scenarios.

Keywords: Hydrodynamic Load, Dam Break Wave, CFD, RANS

CONTENTS

List of Figures

List of Tables

Acronyms

2D	two-dimensional
3D	three-dimensional
CFD	Computational Fluid Dynamics
CFL	Courant-Friedrichs-Lewy Condition / Number
DNS	direct numerical simulation
LES	large eddy simulation
RANS(E)	Reynolds-averaged Navier-Stokes equations
SST	shear stress transport
VNK2	Veiligheid Nederland in Kaart 2

List of Symbols

b	flume width [m]
b	body forces per unit mass
b'	flume width (for symmetry approach) [m]
B	empirical constant (in log-law of the wall)
B	residence width [m]
B'	effective residence width [m]
CFL	Courant Number
E	total energy [J]
Fr	Froude Number
g	gravity acceleration [m/s^2]
h	vertical water height [m]
h_f	water level in flume [m]
h_0	water level in reservoir [m]
h_2	water level bore (Chanson) [m]
k	turbulent kinetic energy [m^2/s^2]
L	residence length [m]
p	pressure [N/m^2] or for equivalent pressure [m] by p/gρ
$\dot{Q}$	heat flow rate [J/s]
R	blockage ratio
t	time [s]
T	stress tensor
$\overline{u}_t$	mean free flow velocity [m/s]
u_τ	friction velocity [m/s]
u^+	dimensionless velocity
U	velocity vector (in OpenFOAM) [m/s]
v	velocity [m/s]
$\mathbf{v}$	velocity vector
v_i	velocity vector elements (i = 1, 2, 3)
v_2	flow velocity bore (Chanson) [m/s]
v'	fluctuating velocity value
$\overline{v}$	time-averaged velocity [m/s]
$\dot{W}$	power [W]
x	coordinate
x_i	directions in coordinate system (i = 1, 2, 3)
y	wall distance [m]
y^+	dimensionless wall distance
α	orientation angle
α	phase fraction
ε	turbulent energy dissipation rate
ϰ	von Karman constant
λ	scale factor
μ	dynamic viscosity [kg/m/s]
ν	kinematic viscosity [m^2/s]
ν_t	eddy viscosity [m^2/s]
ρ	density [kg/m^3]
ρ_a	density air [kg/m^3]
ρ_w	density water [kg/m^3]
σ	surface tension [N/m]
τ_w	wall shear stress [Pa]
ω	turbulent frequency [1/s]

1 INTRODUCTION

1.1 Motive

Since existent, humans are both dependent on and affected by water. A big part of the world population resides in coastal areas, where the sea sometimes unfolds destructive forces. One of the most known floods in Europe in the past occurred in 1953. A storm surge in the North Sea flooded large areas in the Netherlands, Belgium and England and caused huge devastation and the death of more than 1800 people (Slager 2003). Since this country is affected by flood risk more than other European countries it is essential to gain knowledge about the mechanisms leading to collapse of houses in case of floods.

For the Netherlands there are empirical mortality functions (first developed by Jonkman 2007) to predict the mortality of population directly affected by flooding, depending on dominant flow conditions. The mortality functions are based on data from historical flood events. Because the structural conditions of houses have changed over the years, it may be necessary to investigate the fragility of the current building stock. For a detailed structural research containing collapse mechanisms, the resulting loads on buildings in case of floods – depending on flow velocity, water height, building orientation, width and height etc. – should be known.

1.2 Research Task

Currently, researchers put a lot of effort into investigating stability and collapse mechanisms of buildings and residences in floods (see 1.3.5). Jansen (2019) contributes to this research area in her Master Thesis "Structural damage to Dutch terraced houses due to flood actions" by determining what flood conditions can cause structural damage to residential structures. The focus is on the collapse of residences and failure mechanisms. During this research work, physical experiments in model scale were conducted to identify the resulting loads on buildings with a typical Dutch geometry. During those experiments a dam break wave is generated, hitting the residence model. The resulting pressure of the quasi-steady part is measured for certain initial conditions and building orientations.

Those physical experiments serve as a starting point for the present project. The main intention of this work is to build up a numerical model of those experiments. This model then can be accordingly used as a tool to conduct further experiments, enabling the determination of resulting loads on specific building geometries and arrangements under various initial conditions. In detail this includes following tasks:

I) **Numerical Model Setup**

The object is to *develop a three-dimensional numerical model setup*, which allows numerical experiments to be conducted with moderate computational cost. Therefore, the calculations will be based on the Reynolds-averaged Navier-Stokes equations (RANS). This approach includes following elements that should be considered: identification of an appropriate grid size, meshing of the relevant experiment domain, implementing a turbulence model, setting initial conditions, setting boundary conditions, ensuring solution stability, identification and adherence of given model restraints (e.g. regarding near-wall treatment).

II) **Model Validation**

The RANSE-approach allows the usage of a relative coarse mesh and requires the implementation of an appropriate turbulence model. Due to that and since the simulated dam break wave is highly dynamic (large range in flow velocity during one experiment run), the obtained results have to be checked carefully and it is very important to *evaluate the model validity*. By comparing the numerical model results with physical results from Jansen (2019), the accuracy, reliability and validity will be examined. Like in Jansen (2019), the focus is on the quasi-steady part of the dam break wave.

III) **Further Experiment Setups**

The numerical model can be used to extend the range of model setups and to conduct further experiments. The object is to *depict and demonstrate exemplarily how the range of model setups can be extended*. For instance, it can be investigated how flow develops around buildings of different constitutions, dimensions, orientations, shapes, etc. under various input flow conditions. It is also possible to vary the scale and conduct experiments in prototype scale, or to determine the dependency between blockage ratio (~distance to neighboured buildings, urban density) and resulting loads.

In summary, this project aims to provide a numerical model which can be used to determine the quasi-steady load of dam break waves on impervious and rigid residence models. Its validity and accuracy will be examined. The model is intended to be able to investigate the relation between input flow conditions – especially flow velocity and flow depth – and the resulting load on building geometries. In further steps, the results generated by this model could be inserted in structural models to analyse the impact of particular flood conditions on structural stability.

1.3 Quantifying the Risk and Effect of Floods

In this chapter a literature review is given on how the risk and effect of floods is determined, quantified and investigated – especially in the Netherlands –; how experiments can be conducted to gain information about hydraulic load on buildings, and what needs to be considered when conducting such experiments physically and numerically.

1.3.1 Impact of floods: Flood Risk in the Netherlands

In the Netherlands, there is a system established to determine the flood risk for all areas around the country, developed in the VNK2-project (Veiligheid Nederland in Kaart 2). The approach allows to estimate the flood risk for all major levee systems by calculating both probabilities of flooding and its associated consequences (VNK2 2012). For the consequence estimation the flood propagation is modelled and the economic damage and number of fatalities are calculated by using a consequence model. The fatality estimation includes e.g. the mortality functions developed by Jonkman (2007).

Mortality is defined as fraction of fatalities amongst the exposed population (Jonkman 2007). The functions provide mortality depending on flood characteristics (water depth, flow velocity, water level rise rate). The flooded area is classified into four hazard zones depending on the flood characteristics, for each zone there is a function to determine the mortality. A figure of those mortality functions per zone can be found in the appendix on p. 39. The functions are based on information about floods between 1934 and 1965. For this reason it may be necessary to develop an approach which takes possible changes in building quality into account.

1.3.2 Dam Break Wave

The dam break wave has been studied extensively, since it is easy to generate in experiment facilities. It enables to investigate loads on walls or other structures induced by bores and surges in case of floods. Early and most known investigations were developed by August Ritter (1892), who presented the theory of the dam break wave for a horizontal channel. On one side of the channel a reservoir contains water with a depth of h_0 and was considered to be infinite long. The model describes the water surface evolution after releasing the water reservoir h_0. In a coordinate system of x being the horizontal distance to the reservoir front and h the vertical water height, the Ritter solution for the water profile and time averaged velocity v is as follows (Ritter 1892):

$$h(x,t,h_0) = 3^{-2} g^{-1} \left(2\sqrt{gh_0} - xt^{-1}\right)^2 \qquad \text{Eq. (1.1)}$$

$$v(x,t,h_0) = 2/3 \cdot \left(\sqrt{gh_0} + xt^{-1}\right) \qquad \text{Eq. (1.2)}$$

The water surface is of parabolic shape. This is an idealised description, experiments contradict the current procedure, but Ritter's solution reproduces the general features of a dam break wave well (Lauber and Hager 1998). Later the weaknesses of the Ritter solution have been investigated on, because the real wave structure differs especially in the evolution of positive and negative wave fronts (see Castro-Orgaz and Chanson 2017; Chanson 2006). Also the propagation of a surge on dry beds has different behaviour than a surge propagating on a wet bed initially covered with water of $h_f < h_0$ as shown in the following figure.

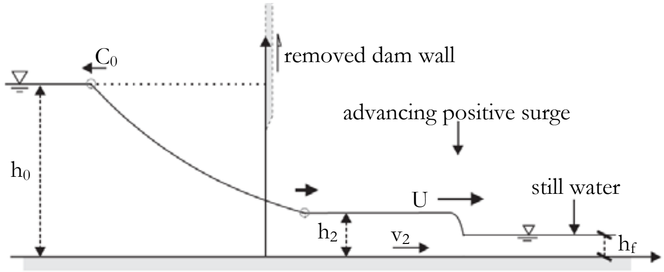

Fig. 1-1 Ideal dam break wave with initial downstream water level (Chanson 2004)

For the resulting water height h_2 and the flow velocity v_2 of the propagating bore following equations have been found to give good agreements with experiments for determining the water height of the propagating bore and its flow velocity (Chanson 2004):

$$h_2 = 0.9319671\left(h_f h_0^{-1}\right)^{0.371396} \qquad \text{Eq. (1.3)}$$

$$v_2 = 2\sqrt{gh_0} - 2\sqrt{gh_2} \qquad \text{Eq. (1.4)}$$

As stated in Wüthrich et al. (2018), a dry bed surge is usually representative of the first incoming tsunami-induced inundation, whereas a wet bed bore may represent following tsunami waves. Wet bed bores are associated with a sudden rise in flow depth, followed by a relatively constant water level h_2. Contrary to dry bed surges wet bed bores have greater wave heights for the same initial release condition, but lower front velocities than dry bed surges (Wüthrich et al. 2018).

1.3.3 Hydrostatic and Hydrodynamic Load on Structures

An obstacle like a residence or wall in a flood is exposed generally to two different load types: hydrostatic and hydrodynamic load. The hydrostatic load on the front side – lateral pressure – is caused by the water's presence, resulting from different water heights in the front and behind the obstacle. Also the buoyancy belongs to the static load, acting on the obstacle's horizontal wall. Hydrodynamic loads in flood events are caused by the water's motion. They can be distinguished – as depicted by Cuomo et al. (2009) – into *quasi-steady drag / velocity-dominated loads* (including flash floods away from source, debris flows away from source, etc.) and *inertia / acceleration-dominated impulsive loads* (including above mentioned flood events, but close to source). Hydrodynamic loads are a combination of both and depend on the flow kinematic and the geometrical characteristics of the obstacle (Cuomo et al. 2009).

A typical time-history of the dam break wave-induced forces acting on the front side of an obstacle shows a relative sharp peak at the first strike (inertia-dominated) and after that a lower, but longer lasting load (quasi-static part of the flow, see e.g. Fig. 1-3 on p. 10).

This work focuses on the quasi-steady part of the incoming dam break wave. Thus the water height and the flow velocity are the main driving quantities for the load magnitude.

1.3.4 Flow over Surfaces

It is essential to know about the interaction between flow conditions and ground properties, when performing physical or numerical experiments on flood events. Especially in numerical simulations there are several modelling techniques to deal with the flow conditions at rigid boundary wall layers. Whenever there is turbulent flow over a surface, its properties like rough- and smoothness are affecting the way the overflow and the turbulence in the near-wall-region develop. The near-wall velocity profile in turbulent flows can be separated generally into three regions: (1) viscous sublayer, (2) defect layer (also buffer or intermediate layer) and (3) logarithmic layer (Kalitzin et al. 2005). In all layers the flow behaves different. In (1), the layer closest to the wall, the fluid is dominated by the viscous effect and it can be assumed that the fluid shear stress is equal to the wall shear stress (Liu 2016). The flow is basically laminar (Ferziger et al. 2020). In (3) the turbulence stress dominates the flow and the velocity profile varies, following a logarithmic law (Liu 2016). The layer in between (2) is a transition area where both effects exist. To generalise this near-wall flow velocity behaviour following dimensionless variables are used. The velocity is scaled as follows (eg. Ferziger et al. 2020):

$$u^+ = \frac{\overline{u}_t}{u_\tau} \qquad \text{with } u_\tau = \sqrt{\tau_w / \rho}\,, \qquad \textit{Eq. (1.5)}$$

where $\overline{u}_t$ is the mean free flow velocity, u_τ the friction velocity, obtained with the wall shear stress τ_w. The dimensionless distance from the wall is then defined as follows:

$$y^+ = \frac{\rho u_\tau y}{\mu}, \qquad \textit{Eq. (1.6)}$$

where y is the absolute distance from wall in normal direction and μ is the dynamic viscosity. According to Fig. 1-2 the layers are classifiable as follows (Schlichting and Gersten 2017): viscous sublayer is in $0 \le y^+ < 5$, buffer layer in $5 \le y^+ < 70$ and logarithmic layer in $70 \le y^+$. For the logarithmic layer the so called logarithmic law of the wall is applicable:

$$u^+ = \frac{1}{\kappa} \ln y^+ + B, \qquad \textit{Eq. (1.7)}$$

where κ is the von Karman constant and B is an empirical constant. The velocity at the wall is assumed to be zero (no-slip condition). This law has been confirmed by many experiments; it has been found κ to be 0.41 and B around 5.2 for dynamically smooth boundaries with no-slip condition (Ferziger et al. 2020). Although newer research work suggests that the law is not as universal as once was thought, it is applied in many cases (Ferziger et al. 2020).

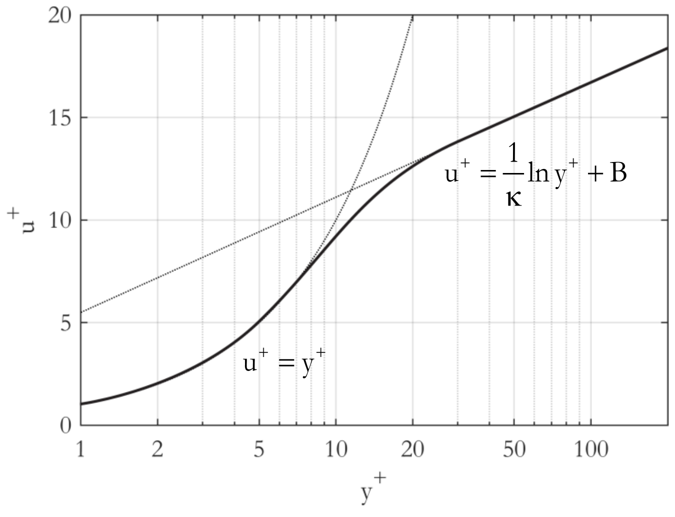

Fig. 1-2 Dimensionless velocity profile in the near-wall boundary layer (Ferziger and Perić 2008)

This knowledge about the near-wall flow conditions is important for CFD-modelling, since the boundary layer, especially the viscous sublayer, is very thin respective the aspired grid cell sizes in most simulations. To resolve this near-wall flow behaviour adequately, either a very high number of thin grid cells would be necessary, or a special wall treatment is needed. In CFD this can be done by using wall functions: From the log-law and a few other assumptions, it is possible to derive a relationship between wall shear stress and the velocity at a point in the logarithmic part of the profile (Ferziger et al. 2020), which will be then adjusted by these functions (see 2.3.2).

1.3.5 Past Studies

A lot of research effort has been put into the determination of hydraulic load of floods on free standing walls or buildings based on *physical* experiments. To list some of them: Ramsden (1996) measures forces on vertical impervious walls under surges on a dry bed, Foster et al. (2017) present equations for predicting forces on rectangular buildings impinged by nominally unsteady tsunami inundation flows, Nouri et al. (2010) and Shafiei et al. (2016) measure dam break wave-induced pressures on various free standing structures with various orientation angles, Wüthrich et al. (2018) investigate the effect of openings in buildings on horizontal forces and tilting moments for dry bed surges and wet bed surges in physical experiments.

Jansen (2019) also conducts physical experiments to measure the quasi-steady load on a residence generated by a dam break wave propagating on a wet bed. She concentrates on a residence with typical Dutch dimensions, with different orientation angles and three flow conditions. The numerical model developed in this project work will be based on her experiments; hence the experiments will be presented in detail in chapter 3.1.

There also have been some *numerical* studies of the hydraulic load on buildings / obstacles under the impact of dam break waves; but the number of numerical investigations with similar research objectives is less than investigations with physical experiments. Aureli et al. (2015) compare several numerical modelling techniques to calculate the impact forces of a dam break wave on a rectangular obstacle, evaluating the results by comparing it to physical experimental data. Amongst others, a three-dimensional two-phase model based on Reynolds-averaged Navier-Stokes equations (see chapter 2.3) is tested. Also Larocque et al. (2013) and Kleefsman et al. (2005) simulate a dam-break flow with a three-dimensional numerical model and compare it to physical experimental data. They focus on the execution of one model setup and the accuracy of the obtained results. The authors conclude, that the three-dimensional model results are comparable to physical data (Aureli et al. 2015) and results satisfactorily reproduce the temporal variation of the measured bottom pressure. (Larocque et al. 2013). It has been found that the numerical model tends to overestimate the falling limb of the load hydrograph after the impact for lower initial water depths in the water reservoir (Aureli et al. 2015). This can be also seen in Kleefsman's experiment: In general the graphs are very similar, but between 0.8 and 1.5 seconds (Fig. 1-3) the simulated pressure is higher than originally measured. The numerical model does not reproduce the resulting pressure oscillations of the highly turbulent bore including aeration in detail.

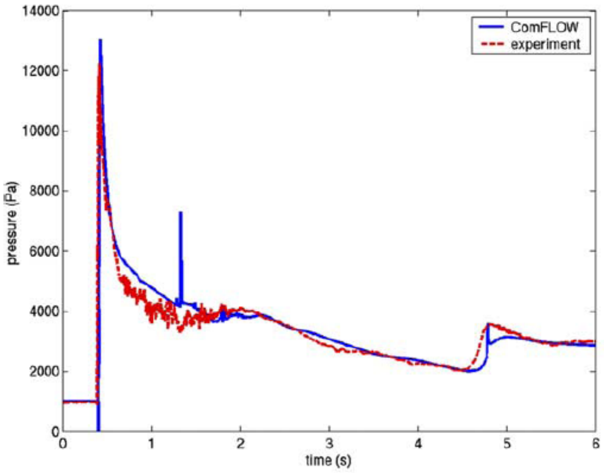

Fig. 1-3 Simulated and measured pressure in Kleefsman et al. (2005)

It can be summarised that numerical models based on three-dimensional Reynolds-averaged Navier-Stokes equations can produce usable results for a dam break wave hitting an obstacle. To a certain extent it is possible to estimate the pressure graph, but in highly turbulent and aerated areas the numerical model tends to overestimate the pressure load. Nevertheless numerical simulations seem to be a strong extension of physical experiments, especially with today's available computing performance. By developing a numerical model a tool can be obtained to assess loads on buildings of different shapes, dimensions, footprints, orientations etc. under various flow conditions.

2 METHODOLOGY

The used numerical properties are depicted in this chapter. Following figure provides a reading guide through the executed tasks within this project work:

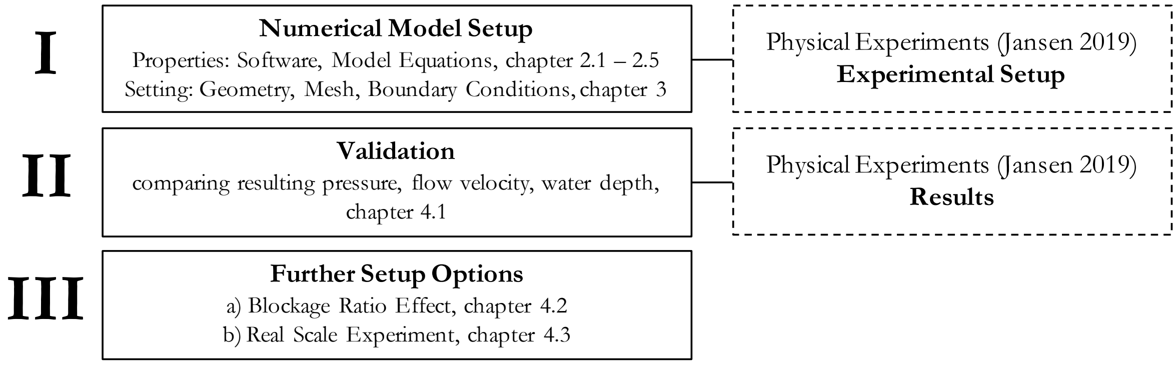

Fig. 2-1 *Tasks and Reading Guide*

For the first working step the physical experiments by Jansen (2019) are implemented into a numerical model. This task includes eliciting suitable boundary conditions, turbulence models and mesh grid sizes. In the second step the validity of the numerical model will be determined by comparing several calculated quantities to measured values. After that (third step) it will be shown how the numerical model can be extended and which objects can be investigated with its help. For instance, the same experiments will be scaled to prototype scale and further initial flow conditions will be applied.

2.1 Software

OpenFOAM (Open Source Field Operation and Manipulation, OpenFOAM 2019) is a non-commercial software package for computational fluid dynamics calculations. The software does not have a graphical user interface, since it consists of C++-libraries, which are used to create executables / applications. This means the calculation process is fully modifiable. The library contains many different applications for pre-processing, solving and post-processing. For instance `blockMesh` and `refineMesh` are applications for mesh generation and manipulation, used in this project during the pre-processing. Employed post-processing applications / functions are e.g. `probes` (writes calculated field values for defined locations into text files) and `yPlus` (calculates y^+-values for wall layers).

Pre-processing applications are responsible for the mesh generation and setup of boundary and initial conditions. All applications are set by preparing code commands in text files ("Dict"-files). When starting an application, it reads the files and implements the commands. The *solver* applications are responsible for the flow calculations; in this project the solver `interFoam` is used. This solver calculates the flow of two immiscible, incompressible and isothermal fluids (OpenFOAM 2019).

Generally a case has an explicit file structure: the folder "*system*" contains text files, where all application properties are set (mesh generation instructions for the pre-processing; turbulence properties, simulation duration, time step for the solver etc.). The folder "*constant*" contains information about the fluid properties and gravity acceleration magnitude and direction. The folder "*0*" contains the initial and boundary conditions and represents the simulation's initial state. When starting the solver, folders will appear continuously, containing all field values / results for each cell. The folders are labelled by the simulation time their contents belong to. Also the folder "*postProcessing*" appears, when post-processing applications are ordered to write out special results.

Within the framework of this project work OpenFOAM v4.1 is used. The calculations are processed on the faculty's high performance computing cluster. The server is accessed by SSH-protocol for command transfer and FTP-protocol for file transfer.

2.2 Way to calculate Flows: Navier-Stokes Equations

The numerical simulations are based on the Navier-Stokes equations. In the context of this project a very brief description of its principles and its quantities should suffice; many details, derivation and scientific depiction can be found in standard texts in literature. Following depictions are mainly gathered from Ferziger et al. (2020). First of all the fluid is characterised as a continuous substance. The driving forces are pressure differences, gravity, shear, rotation and surface tension. Additionally the fluid's macroscopic properties like density and viscosity must be known when studying fluid motion. Also very characteristic is, that the flow properties are affected by the flow speed: At lower velocities / Reynolds numbers the fluid particles follow smooth trajectories (laminar flow), at higher velocities / Reynolds numbers instabilities occur that eventually produce a more random type of flow (turbulence, see 2.3). In some cases also compressibility must be considered, even though for small ratios of flow speed to speed of sound in the fluid the flow may be considered incompressible (Ferziger et al. 2020).

The Navier-Stokes equations, linking all these properties, are based on the fundamental conservation equations in physics: momentum conservation, mass conservation and energy conservation. The **mass conservation** principle

$$\partial \rho / \partial t + \nabla \cdot (\rho \mathbf{v}) = 0 \,, \qquad \textit{Eq. (2.1)}$$

where ρ is the fluid's density, t the time, ∇ the divergence operator and v the velocity vector, expresses the fact that mass will not disappear: The variation of density in time plus variation of mass flow rate have to be zero in a finite volume element. The **momentum conservation** principle is based on Newton's second law; force is equal to mass multiplied by acceleration. The forces which act on the fluid are (1) surface forces – pressure, normal and shear stresses, surface tension etc. and (2) body forces - gravity, centrifugal forces, electromagnetic forces, etc. (Ferziger et al. 2020). For fluids then the equation in differential form is

$$\partial(\rho \mathbf{v}) / \partial t + \nabla \cdot (\rho \mathbf{v}\mathbf{v}) = \nabla \cdot \mathrm{T} + \rho \mathbf{b} \,, \qquad \textit{Eq. (2.2)}$$

where T is the stress tensor (considering normal and shear stress), and b is representing the body forces per unit mass. For the stress tensor further assumptions can be made by using the Newtonian fluid model, which provides relations based on stress being proportional to velocity gradients. The **energy conservation** principle can be expressed as follows (Lecheler 2011):

$$\partial \mathrm{E} / \partial t = \dot{\mathrm{W}} + \dot{\mathrm{Q}} \,, \qquad \textit{Eq. (2.3)}$$

where E is the total energy in the considered fluid element, W the power done on the element and Q the heat flow rate into the element. In most CFD calculations the specific enthalpy is a measure of total energy in the system, thermal conductivity and temperature are quantities of heat flow rate and power is represented by viscous and pressure forces which may be neglected in incompressible flows (Ferziger et al. 2020). However, flow in this project is considered to be incompressible and isothermal. This means fluid density may be assumed constant, compressibility can be neglected and viscosity can be also assumed constant (Ferziger et al. 2020). This reduces the terms which have to be considered in the above conservation equations.

The differential form of the equations can be transformed into other forms, depending on the coordinate system and the way they are intended to be used in further calculations. For most CFD simulations it is common to write the equations in integral form for a finite control volume, which serves as a starting point for numerical calculations (Ferziger et al. 2020). Since there is not a universal analytic solution of the

Navier-Stokes equations they have to be solved numerically. After discretising the domain of interest (eg. with the control volume approach) and building a mesh, the resulting system of equations – after application of initial and boundary conditions – can be solved computationally time step by time step.

In Fig. 2-2 the common fluid flow simulation techniques are shown. First of all, the direct numerical simulation approach (**DNS**) directly solves the native Navier-Stokes equations without any additional assumptions. The difficulty is: to resolve the flow accurately – all eddies of turbulent flow enclosed – the distance between the mesh cells should be smaller than 10e-3 times the geometry of the domain of interest. This usually means about more than 10e9 mesh cells in three dimensional cases, which results in a very large equation system and loads the computers intensively (Martin 2011). This resulted in development of several simulation techniques based on the Navier-Stokes equations, which make compromises of varying extent regarding the accuracy of calculation outcomes. For different areas of application they still can lead to reasonable results, while the computational load is significantly lower.

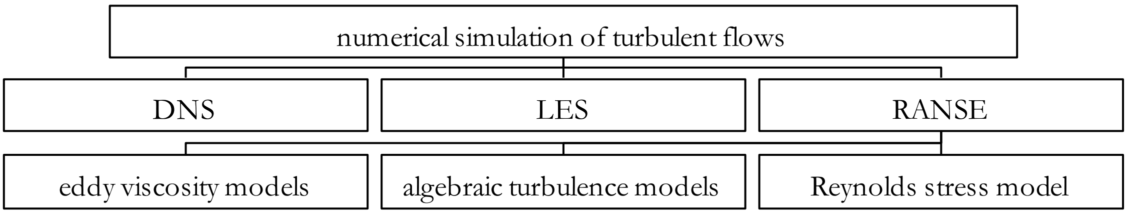

Fig. 2-2 Overview over simulation techniques of turbulent flows (Martin 2011)

Large eddy simulations (**LES**) require a coarser grid than DNS and simulate only large eddies by removing small-scale occurrences by the help of filters. The computational cost is lower than in DNS, but still demanding. The Reynolds-averaged Navier-Stokes equations (**RANSE**) do not calculate the turbulent eddies directly. Its usage allows simulations at relative low computational cost, receiving more general and averaged results of the flow. The effect of spatial and time-variant fluctuating quantities of turbulence on the flow properties then have to be incorporated by the help of turbulence models. There are several techniques (see Fig. 2-2); models based on the eddy viscosity principle are the most used, because they can provide good results at very low computational cost, although the Reynolds stress model seems to provide better results (Martin 2011).

2.3 Deal with Turbulence: Reynolds-Averaging

As mentioned above, in turbulent flows instabilities occur. Jayanti (2018) is describing this phenomenon as follows: Turbulent flow is characterised by highly localised and rapid fluctuations of velocity and pressure, occurring at high Reynolds numbers. These fluctuations are generated in regions of high shear (velocity gradients) such as e.g. near walls by an internal instability mechanism, and then ejected into the bulk motion, thus generated sustained and regulated by the flow itself. The turbulent eddies are present everywhere in the flow domain on average and randomly appear, persist for a time and slowly disappear. Although the typical amplitude of the velocity fluctuations is in the range of one to 10 percent of the mean velocity, their effect on flow can be enormous.

The RANSE approach tends to avoid calculating turbulent eddies since that would require a very fine mesh by solving time-averaged conservation equations. That leads to a loss of information about the fluctuations, but the idea is to obtain averaged results which are adequately representative for the studied flow. The flow quantities like the velocity v are expressed by the sum of a time-averaged value $\overline{v}$ and a fluctuating value v' (Martin 2011):

$$v_i = \overline{v}_i + v_i',$$ *Eq. (2.4)*

where i denotes the axis-direction. By inserting these values into the Navier-Stokes equations, the number of unknown variables increases. The additional terms can be interpreted as Reynolds stresses (Ferziger et al. 2020). To consider the new unknown variables, new equations are necessary: Turbulence models.

2.3.1 Turbulence Modelling

Many turbulence models are based on the eddy viscosity principle: It is assumed, that the effect of turbulence can be represented as an increased viscosity. For the Reynolds stresses the eddy viscosity ν_t is expressed as follows (Ferziger et al. 2020):

$$\overline{v_i' v_j'} = \nu_t \left(\frac{\partial \overline{v}_i}{\partial x_j} + \frac{\partial \overline{v}_j}{\partial x_i} \right) - \frac{2}{3} \delta_{ij} k \, ,$$

Eq. (2.5)

where δ_{ij} is the Kronecker delta and k is the turbulent kinetic energy:

$$k = 0.5 \cdot \overline{v_i v_i}$$

Eq. (2.6)

The eddy viscosity is an artificial value to consider energy dissipation through turbulence, not a physical real quantity. The eddy-viscosity hypothesis is not correct in detail, but can provide reasonably good results for many flows (Ferziger et al. 2020). Following turbulence models provide the eddy viscosity with the help of two equations:

- **k-ε-turbulence model** (by Launder and Sharma 1974):

  This model provides eddy viscosity by using the turbulent kinetic energy k and turbulent energy dissipation rate ε (Schlichting and Gersten 2017):

  $$\nu_t = c_\mu k^2 \varepsilon^{-1} \qquad (\text{with } c_\mu \approx 0.09)$$

  Eq. (2.7)

  The model provides a law for determining ε. Since it is one of the earliest models it is most commonly used (Martin 2011). The model is developed for flow assumed to be in local equilibrium (production and dissipation of turbulence are nearly equal; Ferziger et al. 2020). It has been judged that the model is working very well for highly turbulent flow regions, but does not account for the suppression of turbulence in regions adjacent to a wall (Jayanti 2018). The model tends to an overprediction of the turbulence in flows with adverse pressure gradients like near walls (Menter and Esch 2001) resulting in high wall shear stress and unrealistic high eddy viscosity. This makes the use of wall functions, which adjust the value for ε in near-wall cells, compulsory.

- **k-ω-turbulence model** (by Wilcox 1998)

  Instead of the equation for ε, eddy viscosity is determined by using the turbulent kinetic energy k and a law for the specific dissipation / turbulent frequency ω:

  $$\nu_t = k\omega^{-1}$$

  Eq. (2.8)

  It is said, that the ω-equation has significant advantages near the surface and accurately predicts the turbulent length scale in adverse pressure gradient flows, leading to improved wall shear stress and reduced resolution demands for an integration to the wall (Menter and Esch 2001). This makes this model more applicable for flows near wall layers and its results more stable, but less in inner flow regions (there is a strong sensitivity of the solution to free stream values for ω outside the boundary layer as pointed out by Menter 1994).

- **k-ω-shear stress transport turbulence model** (by Menter 1994)

  The shear stress turbulence model is a combination of the k – ε model and the k – ω model. It utilises the original k – ω model in the inner region of the boundary layer and switches to the standard k – ε model in the outer region (Menter 1994). Thus, the model is intended to collate the advantages of both models.

2.3.2 Wall Treatment Options

Due to the existence of high velocity gradients near walls and high gradients in turbulence and flow behaviour, which are also affecting the properties of the flow outside wall layers, the near-wall flow calculations need careful attention. Especially when using averaged conservation equations, the grid cells are usually not intended to be fine enough for resolving the boundary flow gradients adequately. This is an important reason for the existence of wall functions which allow coarse grid cells and model appropriate flow conditions. Anyway the use of the standard k-ε-turbulence model requires the usage of wall functions, since it overestimates the eddy viscosity at stagnation points (see 2.3.1).

However, in general there are two options how to deal with near-wall flow (which are not arbitrarily combinable regarding grid cell sizes, turbulence models and flow conditions):

a) **Wall Functions**

   They are used to bridge the inner region between the wall and the fully-developed turbulence area to provide near-wall boundary conditions for the conservation and turbulence model equations, rather than to specify those conditions at the wall itself (Liu 2016). Wall functions are typically based on the log-law of the wall for the flow velocity. This allows the computation of the wall shear stress from the values of the wall-parallel velocity component and turbulent kinetic energy at the centre of the near-wall grid cell (Ferziger et al. 2020). For accurate results the centre of the first wall-adjacent cell therefore needs to be located in the log-law area $30 \leq y^+ \leq 200$ of the flow (OpenFOAM 2019) – at any time and any location. This is a very strict constraint which may be violated by the grid configuration often. Additionally, if the cell centre lies in the viscous sublayer, log-law wall functions are generally very inaccurate (Kalitzin et al. 2005) and serious modelling errors may result (Ferziger et al. 2020).

   This led to development of other wall function approaches which try to overcome those strict constraints. So called Low-Reynolds wall functions (Jones and Launder 1973) can provide boundary conditions for grid cells lying in the viscous sublayer, applying other laws than the log-law of the law. For that approach the mesh has to be much finer than for standard wall functions, the first grid cell centre has to be located in the viscous sublayer at around or below $y^+ = 1$ (Kalitzin et al. 2005). There are also adaptive wall functions which calculate the y^+-value to either provide boundary conditions for the log-area or the viscous sublayer (being not universal by ignoring the buffer layer, Liu 2016). One has to consider that very thin cells with a high aspect ratio, which may result at walls, make the solution of discretised equations difficult (Ferziger et al. 2020) and thus could affect the numerical stability negatively (see 2.5.2).

   OpenFOAM includes standard wall functions like `epsilonWallFunction` (for the standard k-ε-turbulence model), `epsilonLowReWallFunction` (adaptive wall function; provides a condition for low- and high-Reynolds number flows; operates in two modes, depending on y^+; OpenFOAM 2019) and `omegaWallFunction` (for turbulence models based on the calculation of specific dissipation ω).

b) **No wall functions**

It is also possible to avoid wall functions by resolving the boundary flow conditions with a very fine grid and applying boundary conditions for pressure (zero gradient) and velocity (no slip condition). For accurate results in the near wall region the viscous sublayer has to be resolved by many cells. Also this approach is only valid if the used turbulence model allows it (k-ε-model does not).

2.4 Two-Phase Flow: interFoam Solver

`InterFoam` is a solver for the flow of two immiscible phases, using a phase-fraction based interface capturing approach (OpenFOAM 2019). It is based on the above described Navier Stokes equations for incompressible and isothermal flow. For considering two phases, air and water, here the density is defined as

$$\rho = \alpha\rho_w + (1-\alpha)\rho_a , \qquad \textit{Eq. (2.9)}$$

where ρ_w is the density of water, ρ_a the density of air and α is the phase fraction, being one inside water, zero for air and varying between zero and one in the interphase region. An additional term in the momentum equation has to consider surface tension; and an additional equation for phase fraction has to be solved in order to locate the phase interface:

$$\partial\alpha / \partial t + \nabla(\mathbf{v}\alpha) = 0 \qquad \textit{Eq. (2.10)}$$

Details about this solver can be found e.g. in Márquez Damián (2010).

2.5 Numerical Setup

2.5.1 Boundary Conditions

All conducted numerical experiments are based on the above depicted RANS equations, together with equations for two-phase flow and a turbulence model, providing eddy viscosity (for selected turbulence model see following chapter).

The densities of water and air are set to $\rho_w = 10^3$ kg/m^3 and $\rho_a = 1$ kg/m^3, their kinematic viscosities to $\nu_w = 10^{-6}$ m^2/s and $\nu_a = 1.48 \cdot 10^{-5}$ m^2/s. The surface tension is set to $\sigma = 0.07$ N/m, gravity acceleration to $g = 9.81$ m/s^2. The text files containing these values are located in the folder "constant".

Initial conditions: The velocity is set to be zero in the whole domain at $t = 0$. The phase fraction value α, which determines the volume amount of water in one volume element, is also set to be zero (air) in the domain. After the mesh is generated, the fraction values for the cells inside the regions, which are intended to be filled with water, are overwritten. Such initial field values are set in the text files in "0".

The domain boundary faces need boundary conditions. Following patch types will be used:

- *symmetryPlane*: This patch type works as a "mirror" and can be used whenever the simulation domain and its results are symmetric along a plane. This reduces needless computation time.
- *patch*: This is a general patch type and thus its effect on the field values needs to be specified. Here it will be used to provide an atmosphere condition at the top of the computed domain. Functions (`inletOutlet`, `pressureInletOutletVelocity`) make sure that both phases can disappear through this boundary and the phase behind this patch is air; pressure is set to be zero at this boundary face.

- *wall*: This patch type is used at impervious walls, especially when wall functions should be applied. Usually the tangential and normal velocity then is set to be zero (see flow over surfaces in 1.3.4) and the pressure to be zero gradient (by the help of function `fixedFluxPressure`). Further specifications are necessary regarding k, ν_t and ε / ω, which will be done by wall functions (see next chapter). This patch type will be used for the flume bottom, flume side and residence.

Before starting a calculation, there need to be made essential specifications in the *controlDict* file. The start and end time needs to be set, also the calculation time step. Since the algorithms of `interFoam` should hold a CFL condition for ensuring convergence in the solution process, maximum CFL-numbers can be set here. The CFL-number depends on the length of one cell and the velocity of the fluid (Courant et al. 1967):

$$\mathrm{CFL} = \Delta t\left(\frac{v_1}{\Delta x_1} + \frac{v_2}{\Delta x_2} + \frac{v_3}{\Delta x_3}\right), \qquad \textit{Eq. (2.11)}$$

where Δt is the time step and v the velocity in the control volume with the length Δx. The solver then adjusts the time step automatically, always keeping the constraints. For a convergence of the inner flow field it is recommended to keep CFL < 1, for a convergence of the algorithm which is responsible for the phase interface, it is recommended to keep CFL < 0.5 (OpenFOAM 2019) at the interface.

2.5.2 Grid Size, Wall Treatment and Turbulence model

As mentioned in 2.3.1 and 2.3.2, the common turbulence models have advantages and disadvantages regarding flow behaviour, especially near walls. Also when conducting numerical simulations of this dam break experiment it turns out, that the used turbulence model, the grid size and the use of wall functions are strongly connected to each other respective the quality and stability of the results. Thus one of these three properties has to be chosen very carefully:

a) **standard k-ε-turbulence model plus standard wall function**:

This is the first tested option. This turbulence model is widely used, due to excellent behaviour in highly turbulent flow regions. The model's weakness at stagnation points near walls (see above) have to be overcome by the use of a wall function, which strictly requires the grid cell centres close to the walls to be in the log-law region ($30 \leq y^+ \leq 200$). Since the mesh is static and the dam break experiment shows high dynamics – initially the velocity is zero in the whole domain; then a bore develops due to high potential energy, with maximum velocity regions, moving across the bottom – it is not possible to hold these restraints at all time and all locations. During the simulation y^+ is both falling below and exceeding the restraints. As described in 2.3.2, serious errors may result, when $y^+ < 30$. Keeping the mesh at the wall in moderate dimensions – to meet the conditions for the most part of the simulation – first seems to show good results. But when refining the mesh in the inner region, the error effect grows, which results in unrealistic flow behaviour. The flow appears more and more viscous. This is why this option was abandoned finally.

b) **k-ε-turbulence model plus wall function for low-Reynolds flow**

In this variant the grid cell centres at the wall layer have to be in the viscous sublayer. This can be accomplished by refining the mesh near the wall. Now, the cells cannot be too thin anymore for accurate results in theory. Two-dimensional experiments showed very good flow behaviour. In return, the increased number of cells affect the computation time significantly. Also it is difficult to keep three-dimensional experiments numerically stable; they tend to crash oftener. Reasons for that may be the cell ratios of near wall cells. Very thin cells could affect the numerical solution process negatively. In addition, Menter and Esch (2001) mention: "in combination with low-Reynolds number extensions, the ε-equation has proven to be numerically stiff, leading to a significant reduction in numerical robustness." This is why this option also was abandoned.

c) **k-ω-shear-stress transport turbulence model plus standard wall function**

This turbulence model was developed to combine the advantages of both the k-ε and k-ω-turbulence model (as described in 2.3.1). The grid cells at the wall boundaries are designed to keep the y^+-range as best as possible (like in a). This time – although the strict wall function restraints are exceeded as well in some parts of the simulation – the results at any grid sizes in the inner domain show very stable behaviour.

Finally the experiments are designed like described in c). It seems to be the best suitable setup, since it also keeps the cell number in a moderate range. The wall function behaviour is correct in a sense that it does not affect the convergence and stability and hence does not "pollute" the results of interest distinguishably. The standard empirical coefficients of the wall function and turbulence model are not changed and can be found in the user guide of OpenFOAM (2019).

Simulations with cubic grid cells of $4 \cdot 4 \cdot 4$ mm^3 or smaller seem to show stable results. As shown in Tab. 2-1, the resulting water depth at the location of the residence at $t \approx 0.9$ s (identified to be in the quasi-steady part) does not change significantly when refining the mesh. Thus the maximum used grid sizes will not exceed 4 mm, in most cases a size of 2.5 mm is used.

Tab. 2-1 Resulting water depths for an exemplary simulation with various grid cell sizes

Cell size	10^3 mm^3	5^3 mm^3	4^3 mm^3	3^3 mm^3	2^3 mm^3
h at t = 0.9	0.0854 m	0.0806 m	0.0786	0.0775	0.0771

3 EXPERIMENTAL SETUP

3.1 Physical Experiments

Jansen (2019) analysed (in "Structural damage to Dutch terraced houses due to flood actions", master thesis) which flood conditions may lead to collapse focusing on current Dutch building stock. The object was to contribute for gaining recent information in order to update the herein before mentioned Dutch Fragility Functions (see 1.3.1). Physical hydraulic experiments in a wave flume were part of the research. The obtained information was used to compare the resulting acting moments with the resistance of the load-bearing walls in further structural analysis. However, here the focus is on the executed physical hydraulic experiments: A dam-break wave was generated, hitting a box which represents the residences in model scale. The resulting quasi-steady load in the form of pressures on different points of the residence was measured which "makes it possible to compare this quasi-steady flood load to the wind load" as provided by the Coastal construction manual (FEMA 2011). Three different flood conditions, two types of residences and five different orientation angles of wave attack were tested (see below). Thus, the pressure coefficient relative to width-to-water depth ratio was determined, depending on the several flow conditions and blockage ratios (ratio of flume width to residence width).

3.1.1 Geometry and Cases

The geometry of the used flume is shown in Fig. 3-1. The water reservoir (left side in the figure) is enclosed by a gate and filled with water to an impoundment depth h_0. When starting the experiment the gate is removed quickly and the flume is flooded. Due to technical reasons the inner part of the flume is filled with a water height of h_f. Thus the dam break wave propagates on a wet bed. The residence of width B and length L is located in the mid of the flume, the firstly hit point always in a distance of 0.50 m to the reservoir gate. Several orientations of the building were tested by varying the orientation angle α. The effective flume width is always adjusted by the use of temporary walls (dashed lines) to keep the blockage ratio $R = B'/b \approx 0.53$ constant in all tests with different orientation angles. The blockage ratio represents the distance to possibly neighboured buildings. In the conducted experiments the maintained blockage ratio corresponds with a various width between the size of a bicycle path or an access road for car drivers, cyclists and pedestrians – depending on the used residence width B and orientation angle (Jansen 2019).

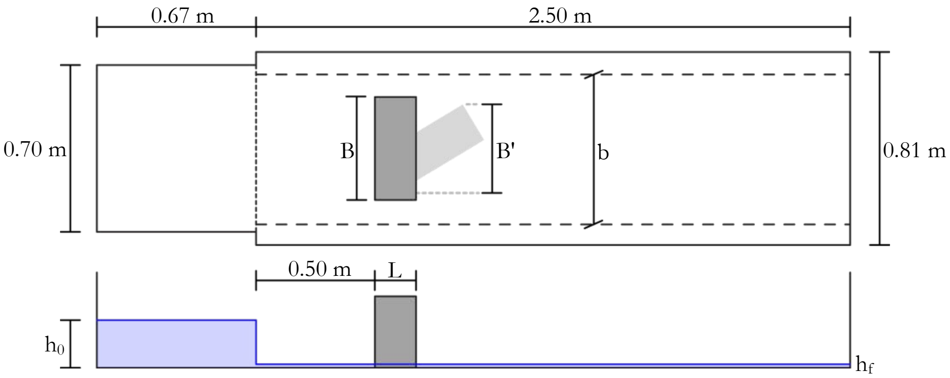

Fig. 3-1 Schematic figure of the flume and experimental setup used in Jansen (2019)

The two residence types had a model width of 43.2 cm and 86.4 cm respectively, both with a length of 17.3 cm. They are representing a group of four or eight residences, modelled by identifying typical Dutch building geometries (Jansen 2019). Thus the two residence types are named "4R" and "8R". Due to the limited maximum width of the flume not all orientation angles could be tested for the long residence type "8R". The conducted test series is listed in the following table:

Tab. 3-1 Test series of conducted physical experiments by Jansen (2019)

	$\alpha = 0°$	**$\alpha = 15°$**	**$\alpha = 45°$**	**$\alpha = 75°$**	**$\alpha = 90°$**
h_0 = 15 cm	4R & 8R	4R	4R	4R	4R & 8R
h_0 = 17.5 cm	4R & 8R	4R	4R	4R	4R & 8R
h_0 = 20 cm	4R & 8R	4R	4R	4R	4R & 8R

To obtain information about the developing free flow field without any residence as a barrier – especially to determine the flow velocity at the location of the building – "baseline" experiments were conducted, where all impoundment depth tests were run without the presence of buildings.

3.1.2 Scaling of the physical model

The hydraulic model is scaled by λ = 1:50. Hence the individual model residence has a base area of 5.4· 8.65 m² and the impoundment depths vary from 7.5 m and 10 m in real scale. The Froude similarity model is used, which means the dimensionless Froude number

$$\mathrm{Fr} = \frac{v}{\sqrt{gL}}, \qquad \textit{Eq. (3.1)}$$

where v is the fluid velocity, g gravity acceleration and L the characteristic length, has to be equal in the model and the reality (see e.g. Chanson 2004). The scale ratios are e.g. 1 for gravity, λ for lengths, $\lambda^{1/2}$ for time and velocity, where λ in this case is 1:50. The fluid and residence material (timber) is not scaled. Remaining scale effects are supposed to be neglectable (Jansen 2019).

3.1.3 Instrumentation and Measuring

Following measuring sensors are applied in Jansen (2019):

- wave gauges for the water height in the water reservoir, in front of the residence and besides the residence; and at the location of the building's front side in the baseline experiments,
- pressure sensors on the residence model, measuring the pressure in central and edge positions at heights of 25 mm and 50 mm (see also appendix p. 39),
- one velocity sensor in the baseline test: at the location of where the residence's front side would be at a height of 1.5 mm to determine the bore's velocity.

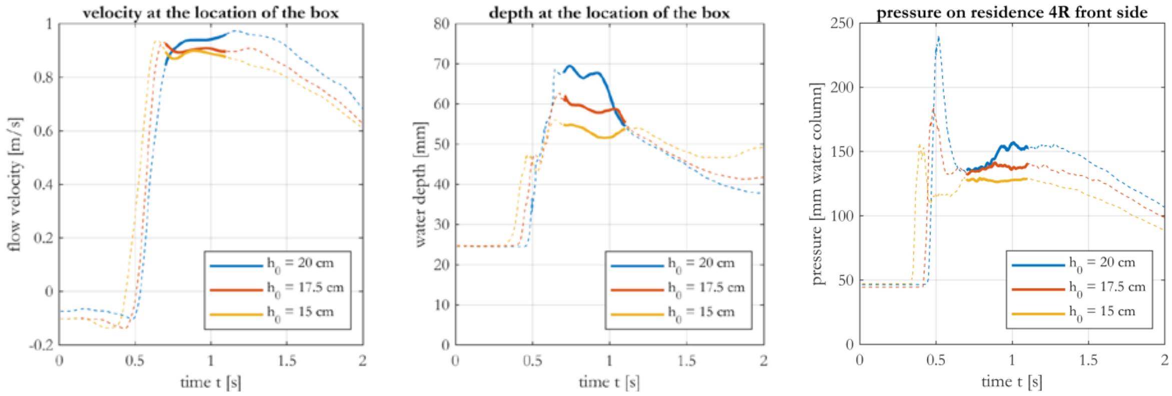

Fig. 3-2 Physical experiments (Jansen 2019): velocity and water depth from baseline test, pressure on residence for 4R, 90°

Fig. 3-2 shows time series for flow velocity and water depth at the location of the building (from baseline tests without buildings) and the measured pressure graph on the residence under same input flow conditions. The quasi-steady part of the flow is identified by Jansen (2019) and marked with bold lines in the range of 0.7 s ≤ t ≤ 1.1 s. The lines represent an average of five test runs.

3.2 Numerical Experiments

The numerical simulations finally are based on the RANS equations (see 2.3), the k-ω-SST turbulence model (see 2.3.1) and wall functions for rigid boundaries as described in chapter 2.5.2. The following chapter describes the implemented geometry, mesh and boundary conditions and lists the conducted experiments.

3.2.1 Geometry Realisation and Boundary Conditions

In general, the simulation domain is of the same dimensions as in the physical experiments. The variable names, as they are used in the case setup files, are shown in Fig. 3-3. But in order to reduce the amount of grid cells, only the essential parts of the experiment are reproduced: The total flume length is not 2.50 m as in the physical experiments; the back flume wall [5] is located 20 cm behind the residence, since only the flow events around the residence are of interest. The flume height is dependent on the initial condition: *flume_x2* = 1.2 · *h_0* to be high enough for the propagating wave.

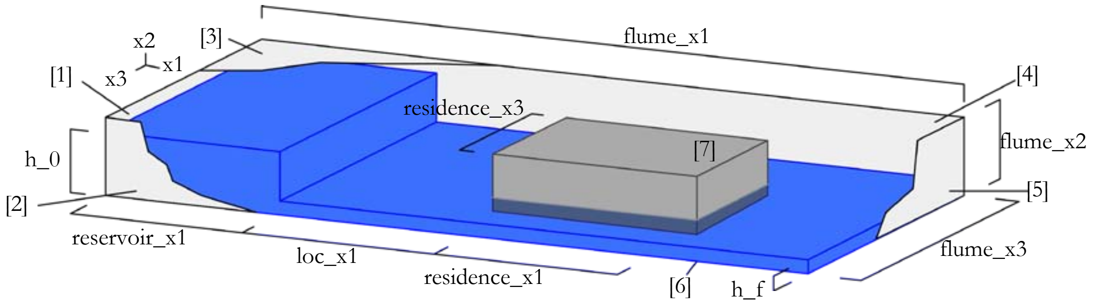

Fig. 3-3 Schematic setup sketch and variables in numerical experiments

The reservoir's front side [1] and the flume bottom [6] are of patch type *wall*, as well as the residence. For the domain's upper side [3] and back flume wall [5] atmospheric conditions are provided (compare 2.5.1). Since the simulation domain is symmetric (for building orientations 0° & 90°), the domain is split and only one half needs to be simulated, providing symmetry boundary conditions along the x_1-x_2-plane through the centreline (`flumemid`). The given boundary patch names and their associated patch types, as they are stated when meshing the domain, are listed in following table:

Tab. 3-2 Numerical model: Boundary patch names and associated types

	boundary patch name	**patch type**
[1]	`inlet`	`wall`
[2], [4]	`sidewall`	`wall (symmetryPlane)`
[3]	`atmosphere`	`patch`
[5]	`outlet`	`patch`
[6]	`bottom`	`wall`
[7]	`residence`	`wall`
	`flumemid`	`symmetryPlane`

The used patch types and their boundary / initial conditions are listed in Tab. 3-3. It contains the keywords as they have to be put into the initial state folder *0*.

The edge between water reservoir and flume (compare Fig. 3-1) is not realised in most simulation cases. On the one hand their effect on the flow when using temporary walls (compare 3.1.1) is assumed to be neglectable; on the other hand the mesh is kept as plain as possible. Only for the cases, where no temporary walls were used in the physical experiments, this edge is realised in the numerical experiments for validation purposes.

Tab. 3-3 Numerical model: Implemented boundary conditions for the different patch types in OpenFOAM

	patch type	**k**	**nut** (ν_t)	**omega** (ω)	**U** (v)	**p**
rigid walls	`wall`	`kqRWall Function`	`nutkWall Function`	`omegaWall Function`	`noSlip`	`fixedFlux Pressure`
atmosphere/ open	`patch`	`inletOutlet`	`calculated`	`inletOutlet`	`pressure InletOutlet Velocity`	`total Pressure (0)`
symmetry	`symmetry Plane`	`symmetry Plane`	`symmetry Plane`	`symmetry Plane`	`symmetry Plane`	`symmetry Plane`

3.2.2 Blockage Ratio Realisation

The flume width *flume_x3* is dependent on the blockage ratio. As mentioned in 3.1.1, the blockage ratio is representative for neighboured buildings and kept constant during the physical experiments at $R \approx 0.53$. Adjacent buildings are represented by the flume sidewalls. In this case the flume width b is determined by Eq. (3.2). In a completely similar numerical realisation then the boundary patch has to be of type `wall`. In the validation simulations it is done this way.

Since the flume sidewall is not an exact realisation of adjacent buildings, it can be assumed that this approach models their effects on the flow only approximately. It would be presumably more realistic to include adjacent buildings into the simulation. In the numerical experiments, symmetry conditions at [2] & [4] can be used to realise the presence of neighbour buildings. When following this approach, b' has to be used for *flume_x3*:

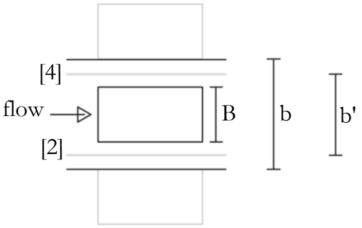

$$b = \frac{B}{R} \qquad \text{Eq. (3.2)}$$

$$b' = \frac{B(1+R)}{2R} \qquad \text{Eq. (3.3)}$$

This approach is recommended for the extended simulations when focusing on the effect of blockage ratio. This is why Tab. 3-2 also lists the patch type `symmetryPlane` for `sidewall`.

3.2.3 Mesh

A fixed Cartesian grid is generated. The main grid cell size of the inner domain is 2.5^3 mm^3, so that in symmetric cases the mesh consists out of 3 to 5 million cells. The wall-normal cell size is adjusted in a range of 0.5 ~ 1 cm, to keep the average value for y^+ in the recommended constraints. Following figures show the three-dimensional meshes schematically (breakdown figure: coarser mesh than finally applied):

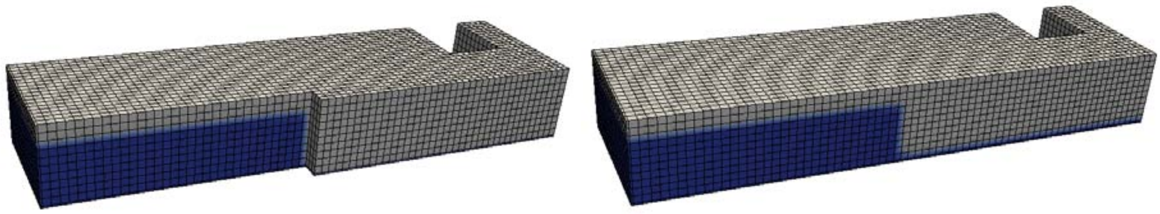

Fig. 3-4 Generated three-dimensional grids (left: validation case, 4R 0°; right: simplified geometry, 4R 0°)

The left figure is showing the mesh for the original validation experiment (containing the water reservoir edge). In the right figure the mesh for the further experiments can be seen. In both figures the domain is symmetric and only one half of the domain is meshed; the initial water height is blue-coloured. The water is propagating from left to right; the front side is the flume sidewall; the non-visible plain in the background is the symmetry plane; the cut-out is representing the residence.

3.2.4 Pre- and post-processing Procedure

Due to the fact that the software OpenFOAM is a library of individual and highly specialised applications, which have to be set and run separately, the executed steps will be summarised here for an overview. Usually all commands for one simulation case will be gathered into one batch text file. Afterwards the computing cluster executes all listed commands successively. An exemplary batch file for one simulation case is shown here:

```
 1 #!/bin/sh
 2 cd ${0%/*} || exit 1
 3 . $WM_PROJECT_DIR/bin/tools/RunFunctions
 4 runApplication blockMesh
 5 runApplication setFields
 6 runApplication decomposePar
 7 mpirun -np 18 renumberMesh -overwrite -parallel
 8 mpirun -np 18 interFoam -parallel | tee log.interFoam
 9 runApplication reconstructPar
10 mv log.interFoam log.interFoamSolver
11 runApplication interFoam -postProcess -func yPlus
```

In line 4 the first application command is actually written. The application `blockMesh` generates the mesh, based on the instructions given in the file `blockMeshDict`. All topological and geometric information about the simulation domain has to be stored here in terms of point, edge and block lists. Because it is inefficient to change the whole code each time when varying the initial conditions (grid size, residence and flume dimensions, etc.), this process is kept flexible by the use of variables. Thus all relevant dimensions have to be assigned in a separate text file named `initialConditions` once.

In line 5 the application `setFields` selects a set of cells – specified in `setFieldsDict` and `initialConditions` – and sets the fluid phase value to $\alpha = 1$. Now the initial hydraulic conditions are applied.

The following command `decomposePar` in line 6 fragments the mesh into several parts, depending on the aspired number of processors. After that (`renumberMesh`, line 7) the remaining cells of those mesh sets will be renumbered by an algorithm, to optimise the band width of the resulting system of equations.

In the line 8 the actual simulation process is started by calling `interFoam`. When using more than one processor, the several processes are managed by the application `mpirun`. In this case 18 processors are requested. The system of equations will now be solved, based on the initial and boundary conditions prepared in the folder *0*. The time step is adjusted automatically to hold the Courant restraints (see 2.5.1).

When the solving process ends and achieves the ending time step (specified in `controlDict`), the command `reconstructPar` rebuilds the fragmented domain (line 9).

After that all calculated field values for each cell of the domain are stored in separate time-labelled folders. Depending on the selected saving frequency, this data can occupy much memory space. This data can now be post-processed, analysed, visualised, etc., e.g. with *ParaView*, a very strong and universal tool for data visualisation, which supports OpenFOAM data. This is useful for checking the mesh generation and simulation results of specific time steps.

In line 11 the post-process-function `yPlus` is executed. It calculates the y^+-values for the wall layers to ensure to be in the recommended range.

In this project the focus is on field data of specified locations, sampled with a high sampling frequency to obtain a time-series. Since storing all results with an appropriate high saving frequency – like described above – would result in a quite unmanageable high data volume, a special function will be included in the simulation process. This function `probes` saves field data (velocity, pressure and phase fraction) for pre-defined locations during run-time and writes it into text files for each calculated time step. For including this function, a list of the locations has to be prepared in the text file `probes` and following command line has to be added in the `controlDict`-file:

```
functions {#includeFunc probes}
```

The results – written by `probes` – will be read and analysed with *Matlab*.

3.2.5 Simulation Cases

As done in the physical experiments, the focus is on the wet-bed propagation ($h_f > 0$). Furthermore the project concentrates on rectangular orientation angles ($\alpha = 0°$, $\alpha = 90°$), since they cause the strongest pressures, which is most relevant for design criteria (Jansen 2019).

The conducted numerical experiments for each working step are listed here:

Tab. 3-4 Numerical Experiments II: Validation

No.	Residence	h_0 [cm]	h_f [mm]	blockage ratio	dimen-sions	grid size [mm]
V1	Baseline	[15 17.5 20]	[16.2 16.8 17.6]	-	3D	2.5
V2	Baseline	[15 17.5 20]	[16.2 16.8 17.6]	-	2D	2.5
V3	4R 0°	[15 17.5 20]	[15 15 15]	0.533	3D	2.5
V4	4R 90°	[15 17.5 20]	[10.8 8.6 7.6]	0.533	3D	2.5

For validation purposes the tests nos. V1, V3 and V4 are based completely on the originally conducted physical tests. The geometry includes the reservoir's edge (see Fig. 3-4 left); the sidewalls are of type `wall`. The baseline tests enable to compare the resulting water depth and flow velocity (at reservoir location), the residence tests allow comparability of resulting pressure loads. The water height h_f is varying in the physical tests in the range between 15 and 20 mm. For the numerical tests, average values for h_f are used.

In addition, one adapted baseline test is conducted. Test no. V2 is simulating a reduced two-dimensional baseline test without any sidewalls, considering the dam-break wave as a pure two-dimensional phenomenon. This could be a logical assumption when planning to perform further numerical tests. Those results can be used to determine the concordance to physical tests.

Tab. 3-5 Numerical Experiments IIIa: Blockage Ratio Tests

No.	Residence	h_0 [cm]	h_f [mm]	blockage ratio	dimen-sions	grid size [mm]
BS1	Baseline	[12.5 15 17.5 20 22.5]	15	-	2D	2.5
BR1	4R 0°	[12.5 15 17.5 20 22.5]	15	0.72	3D	2.5
BR2	4R 0°	[12.5 15 17.5 20 22.5]	15	0.533	3D	2.5
BR3	4R 0°	[12.5 15 17.5 20 22.5]	15	0.3	3D	2.5

Some experiments – considering various blockage ratios – are conducted to demonstrate how the model can be used to determine the effect of urban density on the resulting pressure load. To consider neighboured buildings, sidewalls are realised as symmetry patches (as described in 3.2.2). Besides the original blockage ratio R = 0.533 (test BR2), two additional blockage ratios R = 0.72 and R = 0.3 are included (BR1 & BR3).

Tab. 3-6 Numerical Experiments IIIb: Real Scale Tests

No.	**Residence**	**h_0 [cm]**	**h_f [mm]**	**blockage ratio**	**dimensions**	**grid size [mm]**
BS1	Baseline	[12.5 15 17.5 20 22.5]	15	-	2D	2.5
BS2	Baseline	[625 750 875 1000 1125]	750	-	2D	125
RS1	4R 0°	[12.5 15 17.5 20 22.5]	15	0.533	3D	2.5
RS2	4R 0°	[625 750 875 1000 1125]	750	0.533	3D	125

Finally one test setup will be performed in prototype scale to obtain information about calculated real scale behaviour. The mesh is scaled by factor 50, hence the number of cells is not changing. The water level h_f is kept constant in all tests (1.5 cm small scale, 75 cm prototype scale). The range of input flow conditions (h_0) is enlarged. Both baseline tests (BS1 & BS2) and residence tests (RS1 & RS2) are performed in model and prototype scale.

The provided raw numerical experiment setup data is ordered by the above mentioned test numbers.

4 RESULTS and DISCUSSION

4.1 Validation

4.1.1 Results

Visual Jansen (2019) identifies three different wave impact stages as shown in Fig. 4-1: initial impact, deflection & reflection and quasi-steady part of the flow.

Fig. 4-1 Snapshots of physical experiment (Jansen 2019) – initial impact, deflection & reflection, quasi-steady

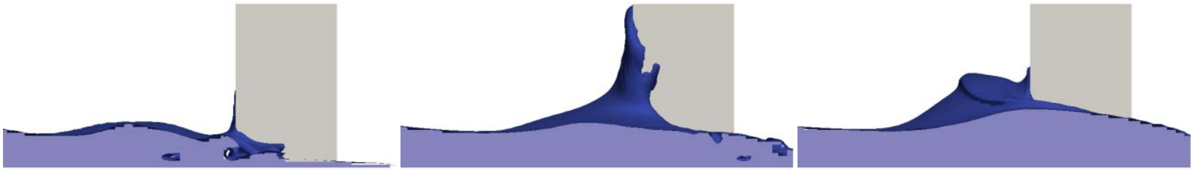

Fig. 4-2 Snapshots of numerical experiment – initial impact, upward-moving jet, begin of quasi-steady period

Fig. 4-2 contains snapshots taken from the numerical simulation, showing similar stages of the wave impact. The first initial wave impact can be seen in the left pictures. This inertia-dominated wave generates high pressures during very short timescales (as also ascertained by Aureli et al. 2015). The pressure graph shows the highest peak value at t ≈ 0.4 s. After that, a jet develops and climbs up the building vertically; simultaneously, the pressure decreases. At a certain point, the water jet starts to detach – decelerated by gravity – and collapses on the water surface (centre picture). This is resulting in a second little pressure peak (visible both in Fig. 4-3 left and right at ≈ 0.6 s, ≈ 0.75 s). A reflected wave develops moving backwards (see right pictures), but from now on the pressure graph is staying constant and then decreasing slowly. As can be seen in the physical experiment snapshots, the wave jet is highly turbulent, the water is strongly aerated and the wave front is disturbed. This may be the reason for irregular pulsations and undulations in the measured pressure graph (Fig. 4-3 left).

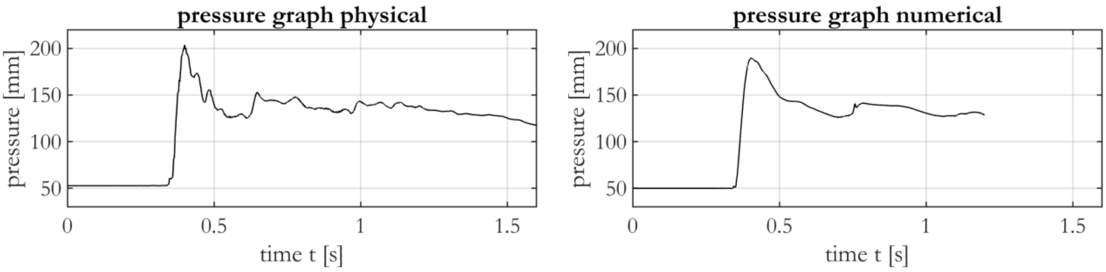

Fig. 4-3 Exemplary pressure graph from one physical realisation (Jansen 2019) vs. numerical experiment (pressure in mm water column)

Pressure The tests V3 and V4 represent simulations of the physical experiments with the residence type 4R. Three impoundment depths h_0 = [15 cm, 17.5 cm, 20 cm] are realised. For comparison between physical and numerical, the measured pressure time-series on the residence's front will be used. The pressure sensor is mounted on the residence centre at a height of 5 cm. The sensor is calibrated in order to measure the equivalent pressure resulting from hydrostatic pressure. Hence, the pressure unit is metre (or millimetre). Pressure values gained from numerical tests are transformed to allow direct comparability. Results from numerical and physical tests are superposed in Fig. 4-4.

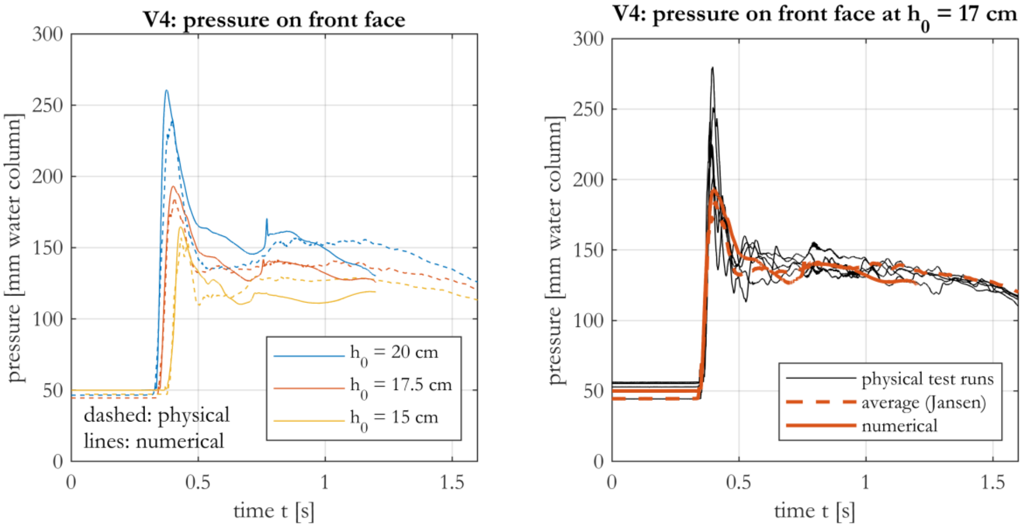

Fig. 4-4 Physical vs. numerical measured pressure for residence type 4R, 90°, simulation V4 (left: dashed lines represent averaged physical measurements; right: all phys. pressure measurement realisations vs. averaged phys. measurement vs. numerical estimation)

Physical results from Jansen (2019) appear as dashed lines. They represent averaged results from five individual test runs. The general shape of the graphs is very similar: both the numerical and physical graph show the abrupt and short initial peak, a trough in pressure when the water jet moves upwards, a pressure rise after that and a second little peak; and a slowly falling limb at the end. For all impoundment depths, the peak values correspond relatively well with each other. Though, the troughs after the peaks are not perfectly matching; the numerical model tends to overestimate the pressure after the first wave impact. The pressure is not decreasing as fast as in the physical tests.

The time-averaged pressure values for the period identified as quasi-steady by Jansen are listed in following table:

Tab. 4-1 Numerical and physical time-averaged pressure values

h_0	physical pressure	numerical pressure	deviation
15 cm	12.8 cm	11.4 cm	10.6 %
17.5 cm	13.7 cm	13.5 cm	1.7 %
20 cm	14.6 cm	15.4 cm	5.5 %

The graphs after the second lower peak value show good agreement for the higher flow conditions, whereas the graphs for the lowest flow condition do not accord with each other well. In this area the numerical model underestimates the pressure.

For a realistic assessment, the right-handed diagram in Fig. 4-4 shows pressure measurements from all 5 equal physical test runs, superposed with the determined average graph by Jansen (2019) and the numerical pressure estimation. The deviations in the physical tests become visible; the numerical pressure estimation is nearly completely within the deviation range. It is also observable, that the physical tests are characterised by many random undulations, which are removed by averaging, while the numerical pressure graph in contrast is rather smooth (see discussion below).

Baseline The baseline tests allow the flow velocity and water depth at the location of the residence to be compared. Those values are needed to characterise the flood flow conditions. Fig. 4-5 shows superposed time-series of numerical and physical baseline tests.

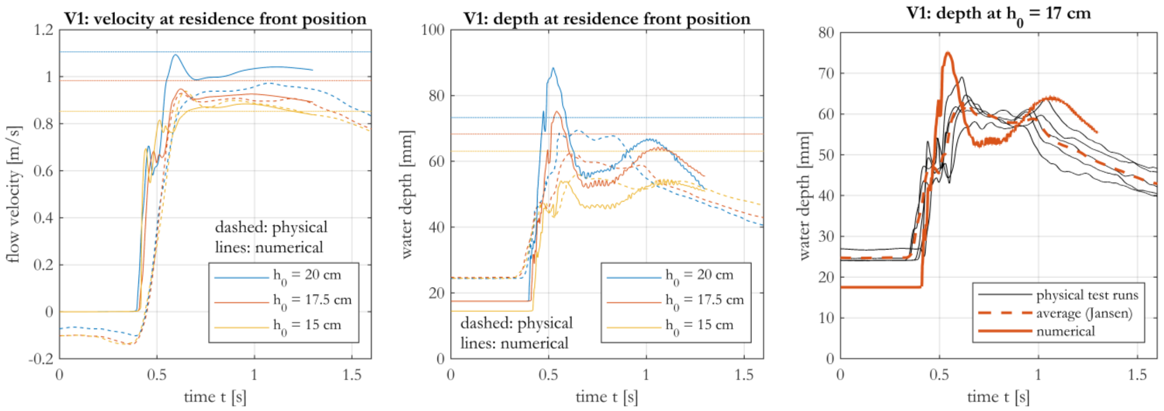

Fig. 4-5 Physically (Jansen 2019) vs. Numerically measured flow velocity and resulting water depths in baseline tests

The physical results, obtained by averaging five test runs, are again represented by dotted lines. It has to be noted that the physically measured values before the wave impact are not meaningful. Both the velocity sensor and the wave gauge give reasonable magnitudes as soon as they are covered with water. The figure also contains horizontal lines for water depth and flow velocity determined by the Chanson model (see chapter 1.3.2).

The measured velocities show very good correlation for h_0 = 15 cm and h_0 = 17.7 cm. After the first wave occurrence at ≈ 0.5 s the graphs are showing a quite stable plateau. The general shapes of numerical and physical results are very similar; the magnitudes after the initial peak are almost at the same level. This is different for h_0 = 20 cm. The averaged graph from the physical tests is much lower than the numerical estimation. At the same time, for this impoundment depth the numerical result is much closer to the Chanson solution. Actually, the Chanson estimations are generally closer to the peak values of the first impact.

For the measured water depths at the residence position (centre diagram) the comparability is complex. The numerical results seem to show a different behaviour than the physical averaged graphs suggest. They show a very significant peak at the beginning and a second peak at t = 1 s. The averaged physical results don't show this behaviour. The peak and the first trough are exceeding respectively falling below the physical graph about the same magnitudes. This means, by averaging peak and trough the physical values would be met nearly exactly. It can be also stated that the second peak magnitude is corresponding well with the physical results in the quasi-steady period.

By plotting all individual physical test run results, it also becomes clear that the two-peak behaviour occurred in reality (right-handed plot), too.

For the quasi-steady period, following table lists the time-averaged values for the physical and numerical experiments:

Tab. 4-2 Numerical and physical time-averaged values for velocity and water depth from baseline tests

h_0	physical v	numerical v	Chanson	physical h	numerical h	Chanson
15 cm	0.89 m/s	0.88 m/s	0.85 m/s	53.1 mm	49.3 mm	63.1 mm
17.5 cm	0.90 m/s	0.92 m/s	0.98 m/s	58.8 mm	56.5 mm	68.3 mm
20 cm	0.93 m/s	1.01 m/s	1.11 m/s	64.8 mm	60.1 mm	73.3 mm

The resulting water depths at the residence location deviate from each other between 3.9 % and 7.3 %. For the lower flow conditions the deviation between numerical and physical result is < 2 %; only for h_0 = 20 cm it is 8.8 %.

4.1.2 Discussion

In this chapter the numerical model results will be discussed, respective to what extent they differ from and equal to physical results. Reasons for discrepancies are quested, to contribute to an evaluation of the numerical model. At the beginning, the numerical conditions and the interrelated expectable constraints are commented on, in order to point out the background, on which the model results evaluation can be based.

Expectable Constraints Since the Reynolds-averaged equations are used, the results do not contain resolved small-scale turbulent fluctuations. Due to the fact that the long-lasting pressure magnitudes and averaged velocities in the quasi-steady part of the flow are focussed, this should not be a limitation for applicability. However, the here presented and widely-used turbulence models were not developed for two-phase flow originally (for further information about this topic see e.g. Kolev 2012); still they are often used together with the approach for fluid interface detection and give usable results for some problems. However, they are not intended to calculate flow quantities in regions, where the interface is highly disturbed and the water is extremely aerated. This disturbance is existent, though, as can be seen in the experiment pictures (Fig. 4-1): in all taken snapshots the water contains air cavitations and the surface of the propagating wave is highly disturbed. The numerical model snapshots illustrate roughly to which extent the air entrapments are reproduced. Besides the fact that the numerical model does not consider possible effects on flow values in highly aerated regions, even the applied mesh cannot be expected to be fine enough to resolve this aeration spatially.

Pressure The pressure measurements from physical experiments are showing a lot of undulations in the graph after the initial impact. This may be due to the highly turbulent character of aerated water splashes; the exact appearance changes in all individual physical test runs. The upwards-moving water jet (defined in 4.1.1) causes various deflections in pressure near its occurrence. The resulting second peak value is appearing at slightly different times and with slightly different magnitudes as can be seen in Fig. 4-4 (right-handed plot). By determining an average graph, the undulations and the second small pressure peaks are not anymore visible. Naturally the numerical model predicts the jet-caused peak always at the same time; this is why it is visible more significantly (Fig. 4-4 left plot). Also, it is conspicuous that the pressure estimation directly after the peak is not decreasing as fast as in the physical tests, only with a short delay. A reason for that may be again the turbulent interphase behaviour which the numerical model is not created for. The numerical water seems to behave a little bit more viscously. Therefore, the pressure estimation for the quasi-steady area seems to work quite well, especially for the lower flow conditions. Only the pressure of the highest tested flow conditions is overestimated by the numerical model. One reason for that may be that the highly aerated bore front and splashing water jet is dissipating more energy in reality than the numerical model is able to consider.

Velocity Like the pressure estimation, the physical and numerical velocity magnitudes are very congruent for both lower flow conditions within the period after the initial impact. Deviations are smaller than two percent. The same reasons as mentioned above could result in an overestimation of the highest flow velocity.

Water depth The resulting water depth at the residence location from baseline tests is complex to evaluate. The numerical graphs are of different shape, they show a clear peak at the initial impact, followed by a trough. The physical averaged graph is not showing such behaviour, whereas a view on the individual test runs shows that in one test this behaviour can be seen as well. One may hypothesise that again the complex structure of strongly mixed fluids at the wave front plays a role. Anyway, the physical behaviour of the initial impact seems to be kind of random to an extent, which does not enable one to compare the graph curve directly. Instead, the numerical graphs show water depths after the trough, which are more congruent to the averaged physical magnitudes. It may be assumable that then the steady part of the flow is reached, even though it is not lasting long due to the finite reservoir length. Time-averaging during the same period as in Jansen's results holds deviations below 8 %.

When conducting two-dimensional baseline tests, the graph is not showing such a high peak. It can be assumed that the flume walls and the flume geometry (water reservoir edges) are responsible for that phenomenon (see appendix p. 40 for 2D-baseline graphs and a visual water surface impression).

Additional remarks Some features have to be mentioned here, which also may limit the range of comparability. Due to technical reasons the initial water depth in the flume h_f was not possible to keep exactly constant for all individual physical test runs. It varies in a range between ~15 and 20 mm in the baseline tests. At the same time, the determined flow quantities are dependent on this initial water height. For illustration, two two-dimensional numerical tests are conducted to show the impact of different initial h_f-conditions. Fig. 4-6 shows the resulting time-series for water depth and flow velocity. The peak difference here amounts 4.5 cm/s for velocity and almost 10 mm for water depth, only resulting from the slightly different initial water depths. This will also affect the resulting pressure magnitude. In the numerical model, the applied mesh also restricts the settable h_f-value, since for the initial state only entire cells can be "filled" with water. Set h_f-values can differ about ± 1.25 mm from aspired values. Also, the applied measurement sensors possibly do not behave in equal measure in pure water conditions (for which they are calibrated) and in highly aerated flow parts.

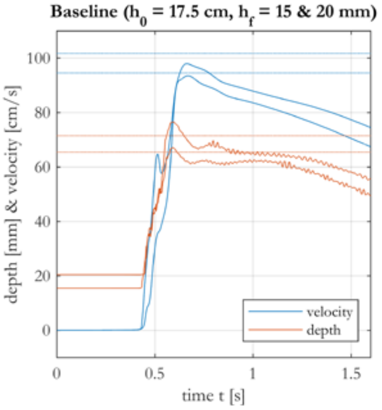

Fig. 4-6 Effects of different initial depths

Summary In general, the averaged values for water depth, velocity and pressure show good congruence in the quasi-steady period defined by Jansen (2019). Deviations between numerical and physical tests remain below 10 %, despite all given model constraints and uncertainties in physical test execution. Most deviations appear in the area of the first wave impact. Reasons for that may be the model constraints described above (respective aeration). For the steady flow part this can be neglected. Maybe one has to reflect about the steady-flow respective definition and duration – possibly a larger water reservoir would make it easier to identify the steady part (see 4.3).

The results document the quality of the numerical model and suggest its applicability for the given problems. Dependencies between flow and load are researchable for the shown conditions. For higher ratios of h_0/h_f the applicability can be questioned, because of the increasing interface turbulence.

4.2 Further Experiments

After comparing numerical results with physical results in equal experiment and flow conditions, some possible manipulations of the numerical model will be shown in the following chapter. They give examples for further possible model applications. For both shown questions neighboured residences will be considered by symmetry planes, not by walls (see 3.2.2). Consequently, driving flow quantities are determined in two-dimensional baseline tests (see attachment p. 40).

4.2.1 Blockage Ratio Effect

Two additional experiment series calculate the resulting pressures for two more blockage ratios. For the present model scale and residence type the available blockage ratios correspond with residence gaps of 25 m (R = 0.3), 9.5 m (R = 0.533 equal to Jansen's tests) and 4.2 m (R = 0.72). For all blockage ratios five different impoundment depths are executed: 12.5 cm, 15 cm, 17.5 cm, 20 cm and 22.5 cm in model scale. Pressure time series for all tested conditions can be found in the appendix on p. 41. The following plot on the left side shows the resulting pressure graphs for the three blockage ratios. The legend entries also include time-averaged values for the black part of the flow. This period is determined as steady part after the initial impact – the same way it was defined by Jansen (2019).

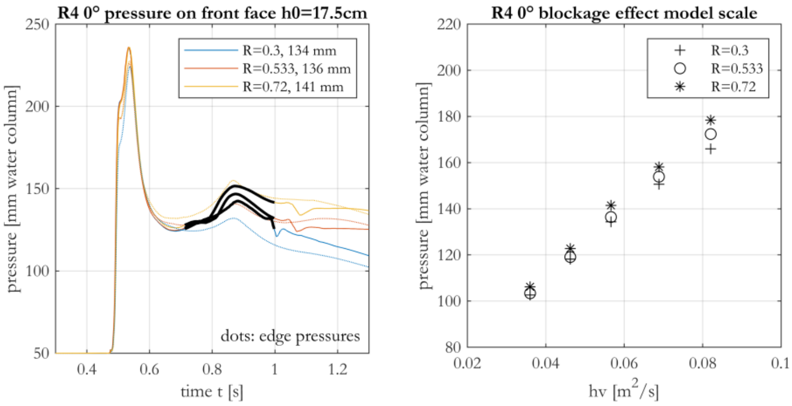

Fig. 4-7 Blockage Effect

As expected, the pressure increases when the blockage ratio increases: a smaller residence gap is retaining the incoming flow and prevents a quick flowing around the residence. The figure is also containing the pressure magnitudes measured on the front residence face's edge (see p. 39).

The figure on the right side is showing the calculated average pressure magnitudes for each blockage ratio by the flow conditions. The flow conditions on the horizontal axis are considered as the product of water depth and flow velocity. The higher this product and the higher the blockage ratio, the higher is the resulting load on the residence front.

It can be seen, that the blockage ratio does not impact the pressure peak values. This is expectable: it is an effect of the first wave impact. The propagating water did not reach the residence gap yet and thus cannot be affected by the blocking ratio. The peak value for the pressure on the residence edge is slightly lower than for the residence centre. After the initial impact, the graphs develop separately: The blocking affects the resulting load.

After the second peaks, the graphs for the two higher urban densities (lower blocking ratio) show a stable plateau. But the blue graph does not stay as constant as the others: this is the test with the largest gap between the residences. Due to that, a larger flow volume can pass the obstacle without being impounded, whereas the initiated flow volume is constant in all experiments.

This leads to important questions: Does the water reservoir have to be adapted for each initial flow and experiment condition? Is the water reservoir large enough to achieve the steady part of the flow? Those questions will be discussed in chapter 4.3.

When considering the resulting pressure within the bold black marked period, for the lower flow conditions the pressure for R = 0.72 is 3.4 % higher than for R = 0.3. For higher flow conditions, the blockage effect seems to grow: For the highest flow conditions the difference between lowest and largest blocking is 7.5 %.

4.2.2 Real Scale Experiments

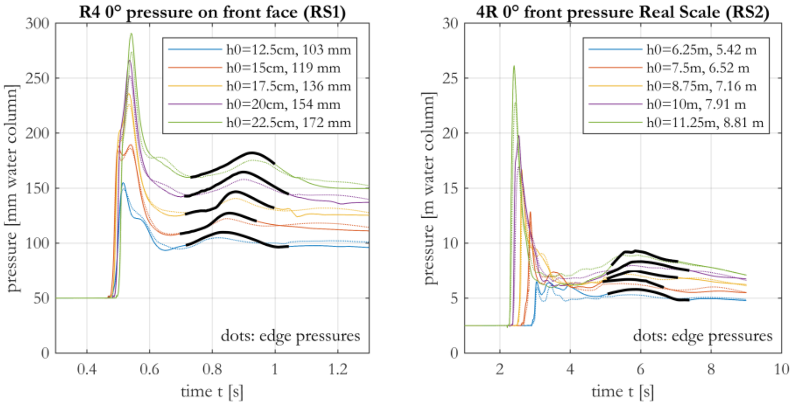

Fig. 4-8 Pressure on residence type 4R in model scale (left) and prototype scale (right)

The figures above contain simulated pressure times for small scale and large scale. The black-coloured periods are identified to be quasi-steady by determining a relatively stable water depth magnitude after the initial peak. Time-averaged values determined for this period are listed in the legend entries.

In both time-series the graphs are of a very similar shape, showing the initial peak, the second smaller peak induced by the returning water jet and a relative stable plateau. The flow velocities and water depths from small and large scale baseline tests are listed in following table:

Tab. 4-3 Flow velocities model scale and large scale from baseline test

h_0 [m]	flow velocity model scale [m/s]	real scale calculated [m/s]	flow velocity real scale [m/s]	deviation
0.125 & 6.25	0.76	5.37	5.50	2.3 %
0.15 & 7.50	0.85	6.01	6.55	9.0 %
0.175 & 8.75	0.92	6.51	7.05	8.4 %
0.200 & 10	0.99	7.00	7.60	8.6 %
0.225 & 11.25	1.08	7.64	8.09	5.9 %

Tab. 4-4 Water depths model scale and large scale from baseline test

h_0 [m]	water depth model scale [m]	real scale calculated [m]	water depth real scale [m]	deviation
0.125 & 6.25	0.048	2.40	2.61	8.8 %
0.15 & 7.50	0.055	2.75	2.83	2.9 %
0.175 & 8.75	0.062	3.10	3.27	5.5 %
0.200 & 10	0.069	3.45	3.70	7.2 %
0.225 & 11.25	0.076	3.80	4.13	8.7 %

The table also contains calculated real scale magnitudes from the small scale experiments by applying the Froude scale model. In this case, the velocity is multiplied by $50^{0.5}$ and dimension by 50.

It is conspicuous that all real scale model values are higher than the values determined by the small scale model and transformed by Froude's scale factors. The magnitude of deviation is not constant; it varies in the range of 2 and 9 percent.

By applying the numerical model in prototype scale one may generate flow conditions directly in real scale. But there are discrepancies when assuming the Froude similarity law. Also, again the above mentioned expectable model constraints should be noted here. It is still unclear, how the turbulent interface interactions and aeration affect the flow conditions in the numerical large scale model with scaled grid cells. Due to that it may be recommendable to do more investigations of the model applicability for real scale questions. Probably, a validation is appropriate to determine its applicability in detail by comparing it to physical large scale experiments. However, the numerical model indicates potential for generating real scale magnitudes.

4.3 Quasi-Steady Period

The conducted numerical experiments are showing that it may be necessary to optimise the quasi-steady flow part identification and definition.

In all experiments, the water reservoir is of equal dimensions. Higher impoundment depths result in higher velocities and higher water depths; due to that the period where a constant water depth can be observed (see centre plot in Fig. 4-8) is shorter. Also, the pressure graphs for lower impoundment depths are showing a better plateau than for higher impoundment depths (see Fig. 4-4). It may be helpful to adapt the reservoir length to the impoundment depth to gain longer steady periods for higher flow conditions and to identify the steady period better. In Fig. 4-9 resulting water depths from two equal experiments are plotted, only differing in the water reservoir size. The magnitude of the steady part becomes obvious. Adapting the reservoir size to impoundment depth and blockage ratio enables to identify the quasi-steady flow part clearly.

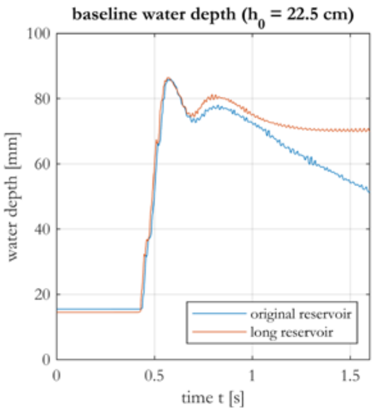

Fig. 4-9 *Effects of water reservoir size*

In addition, the time, when steady-flow conditions start occurring, could be determined separately for baseline tests and pressure determination tests. So far, in this project the pressure was determined for the period when baseline tests – especially the water depth – showed steady conditions. That approach resulted in including the second peaks in the pressure graph. Technically speaking those peaks, generated by the water jet (described in 4.1.1), were still part of initial impact effects. By doing so, the obtained pressure would be more representative for houses near dam breaks in flood conditions with a sudden rise in water level presumably. But for other cases – e.g. slow rising water levels – it could be reasonable to exclude any effects of the first impact when determining resulting pressure loads for quasi-steady periods. For instance, the pressure graphs in Fig. 4-8 are behaving steady after the second peak.

For demonstration, the pressures for the blockage ratio tests were determined at t = 1.25 s which is behind the second peak. Then, the resulting pressures are lower in general, but a stronger dependency on the blockage ratio is observable (see plot in appendix on p. 41).

5 CONCLUSIONS

5.1 Concluding Remarks

It was shown that the RANS-approach including the k-ω-SST-turbulence model and standard wall functions for rigid boundaries can be used to determine the resulting pressure loads on residences for dam break waves. The focus here was on the quasi-steady part of the dam break wave-induced flow after the initial impact for building shapes and flow conditions, which are relevant for the Netherlands (Jansen 2019).

The used turbulence model showed the best applicability for modelling this highly dynamical dam break wave in connection with the two-phase approach, since it links the advantages from the standard k-ε-(good results for inner turbulent flow regions) and the standard k-ω-turbulence model (good behaviour at wall boundaries). Although the constraints for the wall function were exceeded in some parts of the simulation process and violated by the applied mesh, the results within the flow regions of interest showed stable behaviour. The computation time for conducted model-scale three-dimensional experiments of medium flow conditions with the used grid size amounts 2 to 4 hours for one second in the model (20 processors). The longest conducted experiments lasted ~14 hours.

By comparing numerical with physical results from the same experiment setups, the numerical model was evaluated. For the steady state period and the most initial conditions the gained average results (for equal periods) are very comparable and show a maximum deviation of 10 % in the worst case. The dam break physics are reproduced consistently; only the graphs for pressure and water depths show larger deviations directly after the peak. Reasons for that are probably the discussed model constraints for consideration of the physics in strongly mixed fluid interfaces and highly aerated turbulent zones. However, that seems not to affect the results of interest in the later quasi-steady flow part; and the numerical model constitutes an applicable tool for the investigation of flow-induced pressure loads.

To demonstrate the possibilities of model application, further blocking ratio experiments were conducted. That enables to investigate the effect of urban density on the resulting pressure loads on buildings: A relation between flow conditions – represented by the hv-product – and the pressure was obtained. By increasing the blockage ratio, the resulting pressure is increasing; the model is able to show clear dependencies. In this project three different blockage ratios for one building geometry were considered, in further analysis the number of variations can be increased to determine detailed information about the relationship between blockage ratio and pressure coefficients.

The numerical model was modified to determine the aspired flow and load magnitudes in real scale. Therefore the mesh was scaled; the number of grid cells stayed equal. For prototype scale, velocity and height magnitudes are determined, which are up to ten percent higher than calculated values from small scale models based on Froude similarity. Due to that it is assumable that the real scale numerical model needs further analysis and evaluation; regarding the numerical model behaviour in highly aerated interface regions, its effect on the flow, and an appropriate grid size. A validation could help to obtain information about the numerical model behaviour in large scale – especially respective the numerical model constraints and an appropriate grid size.

In summary, it was shown that the numerical model constitutes as a useful tool in addition to physical experiments. In this project, the focus was on model setup and validation. The model can be used to determine further blockage ratio dependencies, building orientations; it is also possible to conduct experiments which include more than one residence in a row to simulate urban region. The calculated pressure magnitudes can be transformed into pressure coefficients according to Jansen's (2019) investigations. Also, 2D planar pressure fields can be extracted from the numerical model for further inserting in structural models as field forces.

5.2 Recommendations

During the conducted simulations, some insights are gained regarding possible model optimisations. When conducting further extensive experiments with numerous parameter variations, it would be appropriate to adapt the water reservoir length to the impoundment depth and blockage ratio (as discussed in 4.3) to ensure the evolution of a steady flow and make it identifiable easier for all conditions. Generally, it could be given consideration to a definition of the steady pressure period after the second lower peak, when aspired to exclude any effects of the first wave impact from the results. By doing so, also the possible numerical model effects respective turbulent aeration should be lower.

As mentioned above, it can be assumed that the real scale experiments with this numerical model need further analysis regarding the model constraints (aerated turbulent interface regions) and an appropriate grid size.

For further analysis, all setup files are provided to reproduce the results and to enable model modifications. A list of provided data and an overview about all recommended steps can be found on p. 42.

BIBLIOGRAPHY

Aureli, Francesca; Dazzi, Susanna; Maranzoni, Andrea; Mignosa, Paolo; Vacondio, Renato (2015): Experimental and numerical evaluation of the force due to the impact of a dam-break wave on a structure. In *Advances in Water Resources* 76, pp. 29–42. DOI: 10.1016/j.advwatres.2014.11.009.

Castro-Orgaz, Oscar; Chanson, Hubert (2017): Ritter's dry-bed dam-break flows: positive and negative wave dynamics. In *Environ Fluid Mech* 17 (4), pp. 665–694. DOI: 10.1007/s10652-017-9512-5.

Chanson, Hubert (2004): Hydraulics of open channel flow: Elsevier.

Chanson, Hubert (Ed.) (2006): Analytical solutions of laminar and turbulent dam break wave.

Courant, R.; Friedrichs, K.; Lewy, H. (1967): On the Partial Difference Equations of Mathematical Physics. In *IBM J. Res. & Dev.* 11 (2), pp. 215–234. DOI: 10.1147/rd.112.0215.

Cuomo, Giovanni; Shams, Gholamreza; Jonkman, Sebastian; van Gelder, Pieter (2009): Hydrodynamic loadings of buildings in floods. In Jane McKee Smith (Ed.): Proceedings of the 31st International Conference Coastal Engineering 2008. Hamburg, Germany. Hackensack, NJ: World Scientific, pp. 3744–3756.

FEMA (Ed.) (2011): Coastal Construction Manual. Principles and practices of planning, siting, designing, constructing and maintaining residential building in coastal areas. Department of Homeland Security. 4th ed. 2 volumes. USA (2).

Ferziger, J. H.; Perić, M. (2008): Numerische Strömungsmechanik. Berlin, Heidelberg: Springer Berlin Heidelberg.

Ferziger, J. H.; Perić, M.; Street, R. L. (2020): Computational Methods for Fluid Dynamics. Cham: Springer International Publishing.

Foster, A.S.J.; Rossetto, T.; Allsop, W. (2017): An experimentally validated approach for evaluating tsunami inundation forces on rectangular buildings. In *Coastal Engineering* 128, pp. 44–57. DOI: 10.1016/j.coastaleng.2017.07.006.

Jansen, Lise (2019): Structural damage to Dutch terraced houses due to flood actions. Master Thesis. TU Delft, Delft.

Jayanti, Sreenivas (2018): Computational Fluid Dynamics for Engineers and Scientists. Dordrecht: Springer Netherlands.

Jones, W. P.; Launder, B. E. (1973): The calculation of low-Reynolds-number phenomena with a two-equation model of turbulence. In *International Journal of Heat and Mass Transfer* 16 (6), pp. 1119–1130. DOI: 10.1016/0017-9310(73)90125-7.

Jonkman, Sebastiaan Nicolaas (2007): Loss of life estimation in flood risk assessment. Theory and applications. [S.l.: s.n.].

Kalitzin, Georgi; Medic, Gorazd; Iaccarino, Gianluca; Durbin, Paul (2005): Near-wall behavior of RANS turbulence models and implications for wall functions. In *Journal of Computational Physics* 204 (1), pp. 265–291. DOI: 10.1016/j.jcp.2004.10.018.

Kleefsman, K.M.T.; Fekken, G.; Veldman, A.E.P.; Iwanowski, B.; Buchner, B. (2005): A Volume-of-Fluid based simulation method for wave impact problems. In *Journal of Computational Physics* 206 (1), pp. 363–393. DOI: 10.1016/j.jcp.2004.12.007.

Kolev, Nikolay Ivanov (2012): Introduction to turbulence of multi-phase flows. In Nikolay Ivanov Kolev (Ed.): Multiphase Flow Dynamics 4. Turbulence, Gas Adsorption and Release, Diesel Fuel Properties, vol. 7. Berlin, Heidelberg: Springer-Verlag Berlin Heidelberg, pp. 39–65.

Larocque, Lindsey Ann; Imran, Jasim; Chaudhry, M. Hanif (2013): 3D numerical simulation of partial breach dam-break flow using the LES and k –ϵ turbulence models. In *Journal of Hydraulic Research* 51 (2), pp. 145–157. DOI: 10.1080/00221686.2012.734862.

Lauber, Guido; Hager, Willi H. (1998): Experiments to dambreak wave: Horizontal channel. In *Journal of Hydraulic Research* 36 (3), pp. 291–307. DOI: 10.1080/00221689809498620.

Launder, B. E.; Sharma, B. I. (1974): Application of the energy-dissipation model of turbulence to the calculation of flow near a spinning disc. In *Letters in Heat and Mass Transfer* 1 (2), pp. 131–137. DOI: 10.1016/0094-4548(74)90150-7.

Lecheler, Stefan (2011): Numerische Strömungsberechnung. Schneller Einstieg durch anschauliche Beispiele. 2., aktualisierte und erweiterte Auflage. Wiesbaden: Vieweg+Teubner Verlag / Springer Fachmedien Wiesbaden GmbH Wiesbaden (Studium). Available online at http://dx.doi.org/10.1007/978-3-8348-8181-6.

Liu, Fangqing (2016): A Thorough Description Of How Wall Functions Are Implemented In OpenFOAM. In *Proceedings of CFD with OpenSource Software.*

Márquez Damián, S. (2010): Description and utilization of interFoam multiphase solver. Final Work. Computational Fluid Dynamics–Facultad de Ingeniería y Ciencias Hidricas, UNL, Santa Fe. Available online at http://infofich.unl.edu.ar/upload/3be0e16065026527477b4b948c4caa7523c8ea52.pdf, checked on 11/9/2019.

Martin, Helmut (2011): Numerische Strömungssimulation in der Hydrodynamik. Berlin, Heidelberg: Springer Berlin Heidelberg.

Menter, F. R. (1994): Two-equation eddy-viscosity turbulence models for engineering applications. In *AIAA Journal* 32 (8), pp. 1598–1605. DOI: 10.2514/3.12149.

Menter, Florian; Esch, Thomas (2001): Elements of industrial heat transfer predictions. In *16th Brazilian Congress of Mechanical Engineering (COBEM)* 109, pp. 117–127.

Nouri, Younes; Nistor, Ioan; Palermo, Dan; Cornett, Andrew (2010): Experimental Investigation of Tsunami Impact on Free Standing Structures. In *Coastal Engineering Journal* 52 (1), pp. 43–70. DOI: 10.1142/S0578563410002117.

OpenFOAM (2019): OpenFOAM User Guide. OpenCFD Ltd (ESI Group). Available online at openfoam.com/documentation/user-guide/.

Ramsden, Jerald D. (1996): Forces on a Vertical Wall due to Long Waves, Bores, and Dry-Bed Surges. In *Journal of Waterway, Port, Coastal, and Ocean Engineering* 122 (3), pp. 134–141. DOI: 10.1061/(ASCE)0733-950X(1996)122:3(134).

Ritter, August (1892): Die Fortpflanzung der Wasserwellen. In *Zeitschrift des Vereines Deutscher Ingenieure* 36 (33), pp. 947–954.

Schlichting, Hermann; Gersten, Klaus (2017): Boundary-Layer Theory. Berlin, Heidelberg: Springer Berlin Heidelberg.

Shafiei, Seyedreza; Melville, Bruce W.; Shamseldin, Asaad Y. (2016): Experimental investigation of tsunami bore impact force and pressure on a square prism. In *Coastal Engineering* 110, pp. 1–16. DOI: 10.1016/j.coastaleng.2015.12.006.

Slager, K.; Wagenaar, D. (2017): Standaardmethode 2017. Schade en slachtoffers als gevolg van overstromingen. Deltares.

Slager, Kees (2003): De ramp. Een reconstructie van de watersnood van 1953. Uitgebr. en herz. versie. Amsterdam: Atlas.

VNK2 (Ed.) (2012): Flood Risk in the Netherlands. VNK2 - The method in brief. VNK2 project office.

Wilcox, David C. (1998): Turbulence modeling for CFD. 2nd ed. La Canada: DCW Industries.

Wüthrich, Davide; Pfister, Michael; Nistor, Ioan; Schleiss, Anton J. (2018): Experimental study on forces exerted on buildings with openings due to extreme hydrodynamic events. In *Coastal Engineering* 140, pp. 72–86. DOI: 10.1016/j.coastaleng.2018.06.002.

APPENDIX

A Mortality Function per Zone

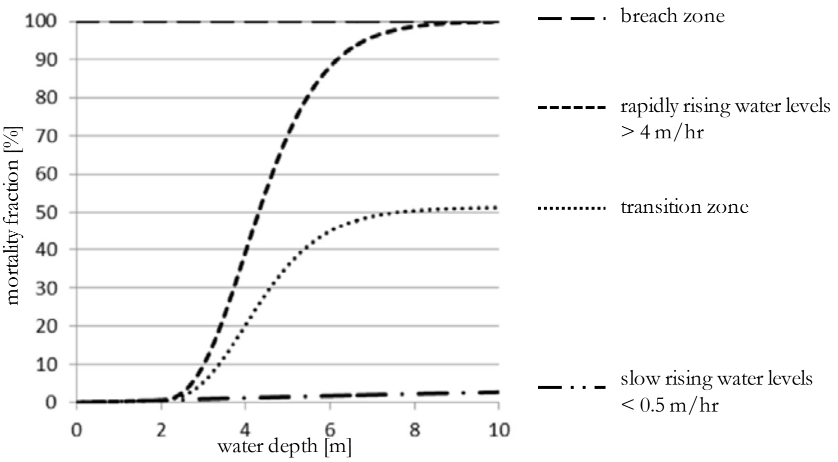

adapted from Slager and Wagenaar (2017)

B Pressure Sensors in Physical Tests

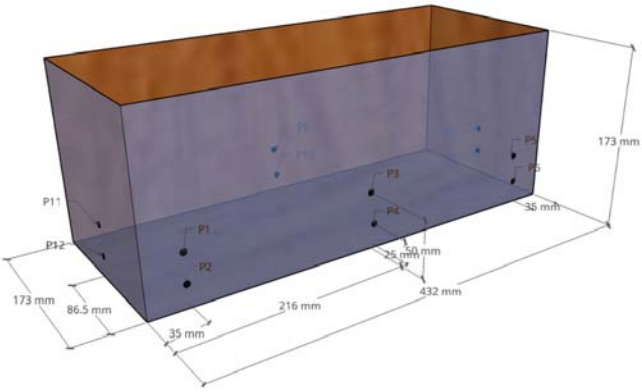

from Jansen (2019)

C Two-dimensional Baseline Test

To consider the dam break wave as a two-dimensional phenomenon, two-dimensional simulations can be used. They show a very stable plateau for the resulting water depth.

Consequently two-dimensional baseline tests will be used for the further simulations.

Following table compares values from this 2D-baseline simulation with physical results.

Numerical and physical time-averaged values for velocity and water depth from baseline tests, simplified 2D baseline

h_0	physical v	numerical v	Chanson	physical h	numerical h	Chanson
15 cm	0.886 m/s	0.835 m/s	0.853 m/s	53.1 mm	54.4 mm	63.1 mm
17.5 cm	0.902 m/s	0.898 m/s	0.983 m/s	58.8 mm	64.2 mm	68.3 mm
20 cm	0.93 m/s	0.994 m/s	1.106 m/s	64.8 mm	72.3 mm	73.3 mm

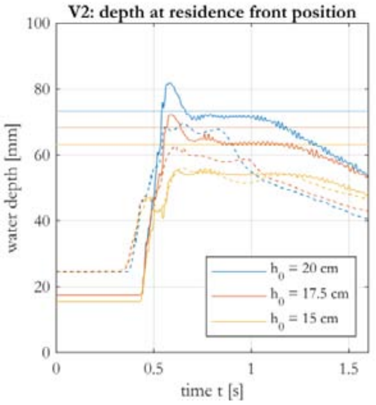

Above: Water depth at residence location from 2D baseline test. Dashed lines: physical results, continuous line: numerical results.

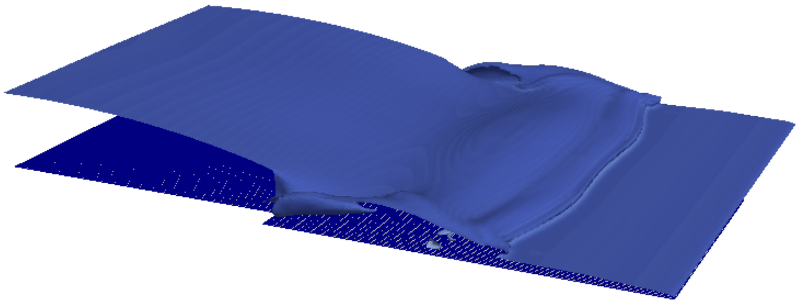

Above: Water surface visualisation for 3D-baseline tests including water reservoir edges at t = 04. s

D Blockage Ratio Effect

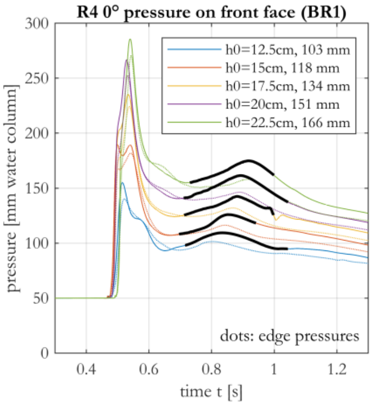

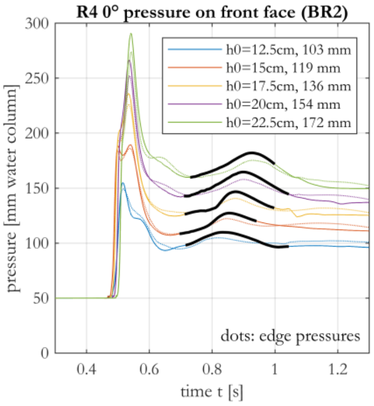

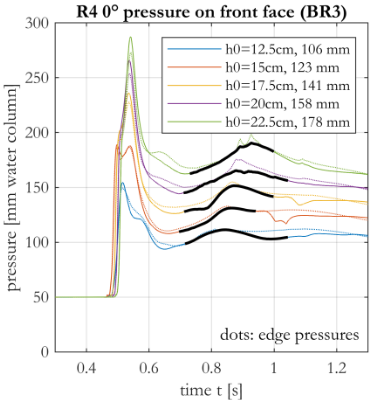

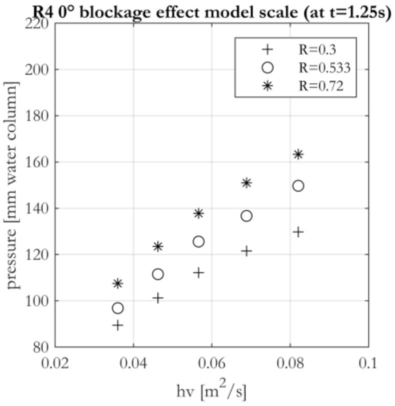

E Processing Steps

1. Set up Dict-Files in folder "system".
    - controlDict: starting time, end time, time step, etc.
    - decomposeParDict: number of processors and instructions on how the mesh is parted for each processor
    - initialConditions: general case-dependent values for geometry and grid size, assigned as variables (e.g. reservoir length, initial water conditions h_0 and h_f, residence dimensions, etc.)
    - blockMeshDict: mesh instructions, geometry, boundary patch types, accesses the variables from initialConditions
    - setFields: where to set water, accesses the variables from initialConditions
    - fvSchemes and fvSolution: configuration of solving schemes
    - probes: coordinates for aspired probe locations. The solver will generate tables during run-time, containing field values for these locations
2. Set up initial and boundary conditions in folder "0".
3. Set up run-file: shown exemplarily in 3.2.4.
4. Set up execution shell-file (if working on a cluster). Executes the run-file.
5. Execute shell file. Now all field values will be written in time-labelled folders. Probe tables will be created in the folder "postProcessing".
6. Use Matlab or ParaView to view and post-process results.

F Provided Simulation Data

The simulation data is arranged in folders labelled by denomination like depicted in Tab. 3-4, Tab. 3-5 and Tab. 3-6. The simulation cases do not contain results, therefore it is recommended to execute them with OpenFOAM.